Developments and Applications of Laser-Based and X-Ray-Based Biomedical Thermoacoustic Imaging Techniques.

by

Hao Lei

A dissertation submitted in partial fulfillment
of the requirements for the degree of
Doctor of Philosophy
(Mechanical Engineering)
in the University of Michigan
2019

Doctoral Committee:

      Professor Jun Ni, Co-Chair
      Professor Xueding Wang, Co-Chair
      Professor Paul Carson
      Associate Professor Kenn Oldham
      Research Assistant Professor Guan Xu

Hao Lei

halei@umich.edu

ORCID iD: 0000-0003-1878-9188

Acknowledgements

I would like to express my sincere gratitude to my advisor Professor Jun Ni for his continuous support, guidance, and encouragement throughout my graduate study and my advisor Professor Xueding Wang for his support, instruction, and supervision of my research. Without them, I would never have had the chance to begin, continue, and complete my research.

I would express my special thanks to Dr. Guan Xu for his valuable suggestions and support for my research. He has always had time to discuss the details of my research and give invaluable pieces of advice.

I would like to express my sincere appreciation to my dissertation committee members, Professor Paul Carson and Professor Kenn Oldham, for their constructive advice and patient guidance during my research and on this dissertation.

I would like to thank Professor Issam El Naqa, Dr. Wei Zhang, Ms. Laura A Johnson, and Dr. Ibrahim Oraiqat for working with me on various projects. All of them have given me a tremendous amount of valuable assistance and expanded my knowledge in their specialized fields.

I wish to thank all my friends and colleagues from S. M. Wu Manufacturing Research Center and Optical Imaging Laboratory. In addition, there are all the other friends I have made, the list is too long to mention all, but their friendships are thankful.

Finally, and most importantly, I want to dedicate this work to my family. The endless love and support from they gave me the confidence to face challenges during these years.

TABLE OF CONTENTS

List of Figures

List of Tables

Abstract

Thermoacoustic imaging (TAI) is one class of biomedical imaging techniques that share the same physical basis, called the thermoacoustic effect (TAE). The TAE phenomenon can be categorized as sonic waves generated following the absorption of energy/heat. In recent decades, as a result of the continuous development of radiation sources such as masers and lasers, the TAE phenomenon has been extensively utilized to achieve biomedical imaging. The hybrid modality offers high contrast and spectroscopic-based specificity image with ultrasonic spatial resolution. It shows great potential for preclinical research and clinical practice in achieving anatomical, functional, and molecular images. So far, however, TAI has not been widely adopted in clinic. The major challenges include 1) the limited imaging depth due to the applied radiation and 2) the difficulty in achieving quantitative image.

The purpose of this research is to further investigate the fundamental mechanism of TAI and to broaden its applications. In the first part of this study, laser-based TAI technique, also known as photoacoustic (PA) imaging, is implemented to improve the diagnosis of Crohn's disease, especially solving the challenge of characterizing the intestinal strictures in bowel. The feasibility of assessing the spatially varying molecular components in *ex vivo* intestinal strictures by obtaining PA molecular component images using a developed acoustic resolution PA microscopy system is validated. Then, the microscopy system is miniaturized to a prototype side-view scanning capsule-shaped probe and its practicability in quantitatively differentiate the

intestinal disease conditions is proved by performing *in vivo* colonoscopy in the rabbit disease model.

In the second part of this study, the potential applications of x-ray-based TAI technique, named x-ray induced acoustic (XA) imaging, are evaluated. Based on soft-tissue phantom studies, the feasibility in monitoring the position of the x-ray beam and measuring the spatially varying dose deposition is validated. These results suggested a potential application of XA imaging method as a novel *in vivo* dosimetric tool in external beam radiotherapy. Furthermore, an XA and ultrasound (US) dual-modality imaging system is established utilizing a commercial ultrasound unit, aiming to obtain XA image and US image simultaneously, both in real time. As demonstrated by the experiments on soft-tissue phantoms, the XA image showing the deposited radiation dose and the US image capturing the motion of target tissue can be naturally co-registered, offering a potential approach for image-guided radiotherapy.

Chapter 1

Introduction

1.1 Background and Motivation

Thermoacoustic imaging (TAI) is one class of biomedical imaging techniques that share the same physical basis, called the thermoacoustic effect (TAE). The TAE phenomenon can be categorized as sonic waves generated following the absorption of energy/heat. The phenomenon was first reported by Alexander Graham Bell in his observations of sound generated by modulated light and in his idea of photophones (Bell 1880). Ideally, electromagnetic (EM) waves from any part of the spectrum or radiation from most energetic particles have the potential to deliver energy/heat and induce thermoacoustic waves. In recent decades, as a result of the continuous development of masers and lasers, the TAE phenomenon has been extensively utilized to achieve biomedical imaging via the benefits of the ultrasonic spatial resolution based on induced acoustic waves and the high contrast due to the absorption of radio frequency (rf) waves (Kruger, Kopecky et al. 1999) and light (from ultraviolet [UV] to near infrared [NIR]) (Xu and Wang 2006). When lasers based on UV to NIR light are applied, the terms *photoacoustic (PA) effect* and *PA imaging* are normally used instead of TAE and TAI.

The general process of thermoacoustic (TA) imaging can be described in four steps (Figure 1-1): (1) pulsed energy is delivered to biological tissues by controlled radiation; (2) part of the delivered energy is absorbed by any kind of absorber and then transferred to the surrounding

1

medium as heat; (3) the local transient temperature increment due to the transferred heat leads to the induced acoustic wave through the TAE; and (4) the induced acoustic wave is detected by an ultrasonic transducer and then processed to produce an image.
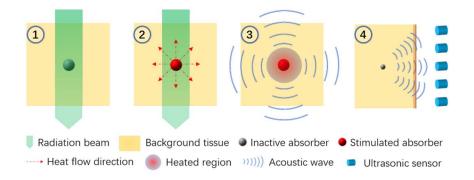
Figure 1-1. Schematic for the general process of TA imaging.

Mostly, nanosecond-pulsed excitation is applied in laser-based TAI for its high pulsed radiation energy and the induced wideband acoustic wave (Wang and Hu 2012). The intensity-modulated continuous wave (CW) laser can also be applied as the radiation source, which may reduce both costs and system size (Maslov and Wang 2008). For rf-based TAI, the pulse duration of the rf source applied is usually in the range of 0.1–1 μs, so that the induced acoustic signal has a broad bandwidth and provides enough spatial resolution (Ku and Wang 2001, Aliroteh, Nan et al. 2016).

By selecting wavelengths of the radiation source, TAI has the potential to differentiate endogenous radiation absorbers, such as hemoglobin (Wang, Pang et al. 2003), melanoma (Oh, Li et al. 2006), DNA/RNA (Yao, Maslov et al. 2010), and cancerous breast tissue (Wang, Bauer et al. 2012), and realize non-invasive functional imaging, such as checking hemoglobin oxygen saturation (sO_2) (Wang, Pang et al. 2003). Meanwhile, by improving radiation energy absorption with particular absorption materials, exogenous contrast agents, such as nanoparticles (De La

Zerda, Zavaleta et al. 2008) and organic dyes (Erpelding, Kim et al. 2010), can be used to enhance image contrast and serve as molecular probes to achieve molecular imaging.

Besides processes related to energy absorption, thermal expansion differences in dissimilar materials have also been utilized to improve image contrast (Tian, Xie et al. 2015) and spatial resolution (Wang, Zhang et al. 2014). Since the thermal expansion process for most bio tissue is temperature-sensitive, TAI can be applied to monitor temperature variations with spatial accuracy during thermal therapy (Shah, Park et al. 2008).

The spatial resolution and imaging depth of the produced image will highly depend on the implementation of TAI. The laser-based microscopic imaging, which is aimed at imaging millimeters deep at micrometer-scale resolution, can be formed by scanning points based on either the focusing of light, named optical resolution photoacoustic microscopy (OR-PAM) (Zhang, Maslov et al. 2012), or the focusing of ultrasound, named acoustic resolution photoacoustic microscopy (AR-PAM) (Zhang, Maslov et al. 2006). Computed tomography, which is based on an array of ultrasound detectors, can cover the larger imaging scale with hundreds of microns of spatial resolution for laser-based TAI, called photoacoustic computed tomography (PACT) (Kim, Erpelding et al. 2010), or rf-based TAI, called thermoacoustic computed tomography (TAT) (Kruger, Kopecky et al. 1999).

TAI, especially PA imaging, shares one advantage with other optical imaging methods: It can spectroscopically measure spatially varying concentrations of chemical components. Moreover, by taking advantage of low ultrasound scattering in soft tissue, photoacoustic imaging (PAI) has the potential to exceed the optical diffusion limit, which restricts the application of most high-resolution optical imaging technologies (Wang 2009). Based on a set of PA images obtained at selected multiple optical wavelengths, quantitatively accurate images of concentration

distributions deep below the tissue surface can be generated, thereby providing an *in vivo* label-free substitute for staining histology. However, the realization of such quantitative PAI is still challenging in both acoustic (non-uniform sound speed, unknown density, non-negligible acoustic attenuation, limited detection bandwidth, and unclarified sensor response) and optical respects (spatially varying thermoacoustic conversion rate and wavelength-dependent fluence) (Cox, Laufer et al. 2009).

Due to the conflict between the demands of high spatial resolution and large imaging depth, an endoscopic version of the PAI system has been developed to allow the imaging probe to be positioned close to the region of interest. Basically, PA endoscopy (PAE) is a miniaturized PA microscopic system, which can deliver light pulses, detect acoustic signals, and achieve effective image scanning inside a confined probe. Most developed prototype PAE systems are based on AR-PAM, whereby spatial resolution can be as good as tens of microns with an imaging depth up to several millimeters (Yang, Maslov et al. 2009, Yang, Favazza et al. 2012, Li, Yang et al. 2014). Due to the point-by-point (angle-by-angle) scanning strategy, however, current PAE systems face problems with motion artifacts in the *in vivo* scenario (Yang, Favazza et al. 2015) and decaying lateral resolution in the axial direction.

Most of the TAI modalities mentioned above require the fluence of radiation pulses, either focused or distributed, to be known or calibrated so that the acquired biomedical imaging features are accurate or quantitative. Alternatively, TAI could be used to monitor spatially varying energy/dose delivery and has the potential to verify the treatment effect induced by some radiation therapies (Bowen 1981). The ionizing radiation used for radiation therapy, such as x-ray photons, electrons, and protons, could also induce the TAE, if the radiation source is pulsed (Bowen, Chen et al. 1991, Tada, Hayakawa et al. 1991) or modulated (Mascarenhas, Vargas et

al. 1984). In 2013, a TA image system based on pulsed x-ray beams generated from a clinical linear accelerator (Linac), named x-ray acoustic (XA) computed tomography (XACT), was demonstrated, successfully imaging a lead rod embedded in chicken breast tissue (Xiang, Han et al. 2013). Lately, in a variety of clinically relevant situations, the feasibility of imaging the Linac-generated x-ray beam shape on pure water and extracting accurate dosimetric information from such images was also demonstrated (Hickling, Lei et al. 2017). These promising works have suggested that XA imaging could serve as an effective dosimetric tool for radiation therapy by relating the intensity of XA images to the local x-ray absorption per mass density, which is commonly referred to as *dose* in radiation therapy. The most dominant challenge to the further application of dosimetric XA imaging is its weak signal, which occurs due to low x-ray absorption in tissue and the special frequency range of XA waves.

In summary, various TAI techniques have great potential for preclinical research and clinical practice in achieving anatomical, functional, and molecular images. So far, however, TAI has not been widely adopted in the clinic. For the applications of laser-based TAI, the realization of accurate quantitative PAI is still challenging due to the complicated mechanism involved during the induced acoustic wave generation and propagation. As a solution of the conflict between the demands of high spatial resolution and large imaging depth, current PAE systems still face problems with motion artifacts in the *in vivo* scenario and decaying lateral resolution in the axial direction. For the applications of x-ray-based TAI, as a potential effective dosimetric tool for radiation therapy, XA imaging technique is suffering from its weak signal and low image quality due to the low x-ray absorption in tissue and the particular frequency range of XA waves from Linacs.

1.2 Research Objectives and Framework

The purpose of this research is to further investigate the fundamental mechanism of TAI and to broaden its applications, especially in (1) characterizing intestinal strictures in Crohn's disease *in vivo* by quantifying relevant histochemical components inside the bowel wall non-invasively using the PAI technique, and in (2) monitoring the performance of dose delivery during radiation therapy conducted by Linac toward achieving *in vivo* dosimetry and image-guided radiotherapy based on the XA imaging technique. The specific research objectives are summarized as follows:

1. Validate the feasibility of assessing the spatially varying molecular components in intestinal strictures of Crohn's disease with a multiwavelength PAI modality: An AR-PAM system is developed to acquire multiwavelength PA images. PA molecular component images showing the relative concentration maps of relevant molecular components are generated. The imaging results are validated by their corresponding histology.

2. Study the practicability of applying an endoscopic AR-PAM system to characterize the intestinal strictures of Crohn's disease *in vivo*: A prototype capsule-shaped AR-PAM probe compatible with clinical endoscopes is developed for characterizing the intestinal strictures. PA molecular component images are generated after resolving several practical problems. Animal validation is conducted on a rabbit trinitrobenzene sulfonic acid (TNBS) disease model through colonoscopy *in vivo*. The obtained quantitative imaging results are statistically analyzed and confirmed by the histopathology.

3. Investigate the feasibility and practical challenges of monitoring the position of the radiation beam and the deposited dose during external beam radiation therapy (EBRT)

by the XA imaging technique. An XACT system is established to achieve XA imaging on soft phantoms made of biological tissue. The potential perturbs and practical challenges in imaging dose distributions with the XA imaging technique are discussed. The sensitivity of XACT in monitoring and quantifying the delivered dose is explored with soft tissue phantoms. The viability of XACT in tracking the position of the radiation dose is demonstrated on soft tissue phantoms.

4. Evaluate the viability in real-time monitoring the misalignment of the treatment beam in relation to the target tissue during EBRT by combining XA imaging technique with established ultrasound (US) imaging modality: An integrated XA and B-mode US dual-modality imaging system is established based on a research ultrasound platform. Phantom studies are conducted to validate the operability in acquiring XA image and the corresponding US image alternatingly in real-time. The practicability in monitoring the alignment of the x-ray beam with respect to the target tissue is evaluated via the experiments on soft phantom. Possible approaches to improve XA imaging quality are evaluated.

This dissertation is organized as follows:

In Chapter 2, a literature review of the TAI technique is presented. Several mechanisms involved in the process, from radiation excitation to induced acoustic detection, are explained. The basic principles of two TAI modalities, scanning microscopy and computed tomography, are introduced. Their corresponding quantitative inverse problems are described.

In Chapter 3, the feasibility of assessing the spatially varying molecular components in intestinal strictures of Crohn's disease by the PAI technique is validated. The basic background

of Crohn's disease and the motivation for applying PAI for its diagnosis are introduced. A prototype AR-PAM system is developed and applied to image human intestinal specimens at multiwavelengths *ex vivo.* The image processing flow, including compensations for the non-uniform fluence distribution of light and the spatial sensitivity of the ultrasound (US) transducer, is presented. The method for generating the PA molecular component images based on multiwavelength PA intensity images is explained. The imaging results are discussed and compared with histology images.

In Chapter 4, the practicability of characterizing the intestinal strictures of Crohn's disease *in vivo* with the endoscopic AR-PAM system is further examined. The motivation and the state of the art of the endoscopic PAM are presented. A prototype endoscopic PAI probe is developed by miniaturizing the scanning head of the AR-PAM into a capsule-shaped side-view imaging probe. The motion artifacts created from intestinal peristalsis are compensated for to improve image quality. A digital refocusing method is applied to overcome the problem of a limited depth of view caused by the highly focused transducer. A TNBS rabbit model of intestinal inflammation and fibrosis is used to perform *in vivo* colonoscopy with the prototype probe. The quantitative chemical component images are obtained, and they agree with the statistical histopathology analysis.

In Chapter 5, the feasibility and practical challenges of monitoring the position of the radiation beam and its deposited dose during external beam radiation therapy via the XA imaging technique are investigated. External beam radiation therapy and *in vivo* dosimetry are presented. A prototype XACT system is established and tested with phantoms made from biological tissues. A physical correlation between absolute dose and XA image intensity is derived, and the challenges in achieving more accurate dose monitoring are addressed. The sensitivity of XACT

in monitoring and quantifying the delivered dose is explored. The potential of XACT in tracking the position of the radiation dose and measuring beam–target misalignments is demonstrated.

In Chapter 6, the viability in real-time monitoring the misalignment of the treatment beam in relation to the target tissue by combining XA imaging technique with established ultrasound (US) imaging modality is evaluated. The motivation and background of image-guided radiation therapy (IGRT) is introduced. An integrated XA and B-mode US dual-modality imaging system established based on a clinically ready research ultrasound platform is presented. Phantom studies are conducted to validate the operability in acquiring XA image and the corresponding US image alternatingly in real-time. Its practicability of tracking the relative movement between treatment x-ray beam and the target tissue is demonstrated. The issues about weak XA signal and limited spatial resolution are discussed and the possible approaches are evaluated.

In Chapter 7, the conclusion is provided. In addition, possible topics for future research work are discussed.

Chapter 2

Review of Thermoacoustic Imaging Techniques

2.1 Theory of Thermoacoustic Wave Generation

Understanding the mechanisms behind thermoacoustic (TA) wave generation is crucial for exploring and simplifying the mathematical model for the physical process from radiation excitation to acoustic wave generation. In this section, the formulation of the forward problem, especially for photoacoustic imaging (PAI) and x-ray acoustic (XA) imaging, is presented, while the assumptions made for its simplification are explained.

2.1.1 Radiation energy delivery and absorption

The techniques of PAI, laser-based thermoacoustic imaging (TAI), typically use EM radiation in the visible or NIR part of the spectrum. The wave properties in this wavelength region are related to the molecular constituents of biological tissues, as EM waves will interact with the tissues and excite vibrations in the molecules (Pasquini 2003). Potential endogenous absorbers, such as hemoglobin, lipids, water, and collagen, have distinctive optical absorption spectra (Figure 2-1).
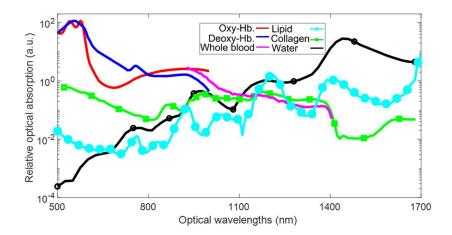
Figure 2-1. Relative optical absorption spectra of major chemical components
in biological tissue.
(Cheong, Prahl et al. 1990, Wang, Chai et al. 2011)

In biological tissues, the scattering of visible and NIR photons is mainly elastic, which means

that EM waves will not change their wavelength during the scattering process. Therefore, the

radiative transport equation (RTE) can be simplified as (Cox, Laufer et al. 2012):

$$\frac{1}{v_c}\frac{\partial\varphi(\boldsymbol{r},\hat{s},t)}{\partial t} + \big(\hat{s}\cdot\nabla + \mu_a(\boldsymbol{r}) + \mu_s(\boldsymbol{r})\big)\varphi(\boldsymbol{r},\hat{s},t) - \mu_s\int\Theta(\hat{s},\hat{s}')\varphi(\boldsymbol{r},\hat{s}',t)d\hat{s}' = q(\boldsymbol{r},\hat{s},t) \quad \text{2-1}$$

where v_c is the speed of the EM wave inside the medium, $\varphi(\boldsymbol{r},\hat{s},t)$ is the radiance intensity in

direction $\hat{s}$ at location $\boldsymbol{r}\in\boldsymbol{R^3}$ and time t, $\Theta(\hat{s},\hat{s}')$ is the scattering phase function describing

the probability that a photon is scattered in direction $\hat{s}$ from direction $\hat{s}'$, μ_a is the absorption

coefficient, μ_s is the scattering coefficient, and $q(\boldsymbol{r},\hat{s},t)$ is the source term of the radiation.

The radiation fluence rate Φ will be the integral of the radiance intensity over all directions $\hat{s}$:

$$\Phi(\boldsymbol{r},t) = \int\varphi(\boldsymbol{r},\hat{s},t)\,d\hat{s} \quad\quad \text{2-2}$$

As the modulated radiation source, usually nanosecond-pulsed, is applied with intensities below the exposure safety limit (American National Standards Institute 2007), all the radiation energy absorbed will transform into heat in the model (Hoelen and Mul 1999):

$$H(\boldsymbol{r}, t) = \mu_a(\boldsymbol{r})\Phi(\boldsymbol{r}, t) \qquad \text{2-3}$$

where $H(\boldsymbol{r}, t)$ is the heat absorption rate at location $\boldsymbol{r} \in \boldsymbol{R}^3$ and time t.

In the case of x-ray radiation, especially the MVs x-ray photon produced by clinical linear accelerators (Linac) for radiation therapy, the photon interacts with an outer-shell orbital electron of an atom primarily through Compton scattering (Gunderson 2015). During this inelastic scattering, the photon is scattered at some angle with reduced energy, while the orbital electron is ejected with kinetic energy equal to the difference between the energy of the incident and the scattered photon. The ejected electrons scatter and deposit energy to the medium over which they traverse. The radiation dose in the radiation therapy is quantified as the amount of energy deposited per unit mass with the unit Gy ($1Gy = 1J/kg$). Most of the deposited energy will ultimately transfer to heat, while some fraction may participate in chemical reactions (Lomax, Folkes et al. 2013) or optical emissions (Glaser, Zhang et al. 2014). Therefore, the temporal dose density D_r can be related to the heat absorption rate H considering a thermal efficiency η_{th}:

$$H(\boldsymbol{r}, t) = \eta_{th}(\boldsymbol{r})\rho(\boldsymbol{r})D_r(\boldsymbol{r}, t) \qquad \text{2-4}$$

where ρ is the mass density of the material at location $\boldsymbol{r} \in \boldsymbol{R}^3$.

2.1.2 Heat transfer and temperature rise

The heat absorption rate $H(\boldsymbol{r}, t)$ defined above cannot be converted to a temperature rise distribution $T(\boldsymbol{r}, t)$ directly, since it only describes the averaged energy rate captured by some

12

absorbers inside a unit volume dr^3 at location r. Instead, each "hot" absorber will transmit the heat to the surrounding medium as a heat pole (Kruger, Liu et al. 1995):

$$\rho(r)C_v(r)\frac{\partial T(r,t)}{\partial t} = \lambda_{th}(r)\nabla^2 T(r,t) + H(r,t) \qquad \text{2-5}$$

where C_v is specific heat capacity at constant volume, and λ_{th} is the thermal conductivity. For the simplest case, in which one absorber acquires energy $H_a(r,t) = E_a\delta(r)\delta(t)$ from radiation and transfers the energy to an isotropic homogenous medium, eq. (2-5) can be solved with Green's function approach:

$$T(r,t) = \frac{E_a}{\rho C_v}\left(\frac{\rho C_v}{4\pi\lambda_{th}t}\right)^{\frac{3}{2}} e^{-r^2\rho C_v/4\lambda_{th}t} \qquad \text{2-6}$$

Therefore, after the time taken for one pulse duration τ_p, the distribution of temperature rise will be confined inside the thermal diffusion distance d_{th}:

$$d_{th} = 2\sqrt{\alpha_{th}\tau_p} \qquad \text{2-7}$$

where $\alpha_{th} = \frac{\lambda_{th}}{\rho C_v}$ is the thermal diffusivity ($\sim 0.15 \ mm^2/s$ for soft tissue) (Welch and Van Gemert 2011). If a nanosecond laser has τ_p and is about $5 \ ns$, d_{th} will be about $55 \ nm$ in soft tissue. The x-ray generated from clinical Linac for radiation therapy is usually $3-6 \ \mu s$ (Kainz 2006, Hickling, Léger et al. 2016), so the corresponding d_{th} is only about $2 \ \mu m$ during the excitation. Since the thermal diffusion distances are much smaller than the scale of spatial resolution and unit volume considered in this study, eq. (2-5) can be rewritten by omitting the first term on the right-hand side:

$$\frac{\partial T(\mathbf{r}, t)}{\partial t} = \frac{H(\mathbf{r}, t)}{\rho(\mathbf{r}) C_v(\mathbf{r})} \qquad \text{2-8}$$

Under this assumption, the average energy rate captured by all absorbers inside a unit volume $d\mathbf{r}^3$ at location $\mathbf{r}$ will be confined and induce the increment of the average temperature in this unit volume.

2.1.3 Thermal expansion and acoustic wave generation

In the isotropic homogeneous medium, the variations of density and pressure due to a small temperature rise inside unit volume $d\mathbf{r}^3$ can be described as (Cox, Laufer et al. 2012):

$$\frac{1}{\rho} \frac{\partial \rho}{\partial t} = \frac{1}{K_T} \frac{\partial p}{\partial t} - \beta \frac{\partial T}{\partial t} \qquad \text{2-9}$$

where p is the internal pressure, K_T is the isothermal bulk modulus, and β is the volumetric thermal expansion coefficient. If the radiation pulse is short enough that the mass density has no time to change, then the left hand side of eq. (2-9) can be set to zero, and the relation between pressure and temperature yields:

$$\frac{\partial p}{\partial t} = \beta K_T \frac{\partial T}{\partial t} \qquad \text{2-10}$$

This constraint of pulse duration τ_s, called stress confinement, is related to the size of the unit volume $d\mathbf{r}^3$, as the variation of mass passing through the medium is limited by the speed of sound v_s:

$$\tau_s = \frac{dr}{v_s} \qquad \text{2-11}$$

14

where dr is a 1D size of the unit volume and the limit of spatial resolution in TAI. Under this stress confinement, the wave equation governing the acoustic wave generation and propagation can be written as:

$$\left(\nabla^2 - \frac{1}{v_s^2}\frac{\partial^2}{\partial t^2}\right)p(r,t) = -\frac{\beta(r)K_T(r)}{v_s^2}\frac{\partial^2 T(r,t)}{\partial t^2}\qquad\text{2-12}$$

By replacing temperature rise $T(r,t)$ with heat absorption rate $H(r,t)$, eq. (2-12) becomes:

$$\left(\nabla^2 - \frac{1}{v_s^2}\frac{\partial^2}{\partial t^2}\right)p(r,t) = -\frac{\beta(r)K_T(r)}{\rho(r)C_v(r)v_s^2}\frac{\partial H(r,t)}{\partial t}\qquad\text{2-13}$$

The solved acoustic wave pressure detected by the transducer at position r and time t can be expressed by:

$$p(r,t) = \frac{1}{4\pi v_s^2}\int dr' \frac{1}{|r-r'|}\Gamma(r')\frac{\partial H(r',t')}{\partial t'}\bigg|_{t'=t-\frac{|r-r'|}{v_s}}\qquad\text{2-14}$$

where Γ is the Grüneisen parameter, defined as:

$$\Gamma(r) = \frac{\beta(r)K_T(r)}{C_v(r)\rho(r)}\qquad\text{2-15}$$

If the radiated medium does not change its properties during the radiation pulse, then the heat absorption rate $H(r,t)$ can be expressed with a spatial distribution and time profile separately:

$$H(r,t) = H_d(r)h_t(t)\qquad\text{2-16}$$

where $h_t(t)$ is the normalized temporal profile of the radiation pulse, and $H_d(r)$ is the spatial distribution of the heat absorption. By taking the ultrasound detector position as the origin of the

coordinates and further considering the spatial response of the ultrasonic detention, eq. (2-14)

becomes:

$$p(t) = \frac{1}{4\pi v_s^2} \int dr \frac{1}{r} p_0(\boldsymbol{r}) h_s(\boldsymbol{r}) \frac{\partial h_t(t')}{\partial t'}\bigg|_{t'=t-\frac{r}{v_s}} \qquad \text{2-17}$$

where $h_s(\boldsymbol{r})$ describes the spatial sensitivity of the ultrasound detector, and $p_0(\boldsymbol{r})$ is the initial

acoustic pressure induced by the radiation pulse:

$$p_0(\boldsymbol{r}) = \Gamma(\boldsymbol{r}) H_d(\boldsymbol{r}) \qquad \text{2-18}$$

2.2 Principles of Thermoacoustic Imaging Modalities

As a biomedical imaging method, TAI uses the detected signal $p(\boldsymbol{r}, t)$ to form an image of

$I(\boldsymbol{r})$, which contains bio information in the region of interest. The fundamental information

generated in TAI is a map of initial acoustic pressure $p_0(\boldsymbol{r})$. In this section, two major classes of

TAI strategies, scanning microscopy and computed tomography, are introduced.

2.2.1 Scanning microscopy

As shown in Figure 2-2, scanning microscopy needs either focused EM fluence or a focused

acoustic detector to limit the field of view in each A-scan acquisition. The axial resolutions in

both cases are determined acoustically and are related to the frequency bandwidth of the applied

ultrasonic sensor. In laser-based TAI, optical focusing is easy to achieve and generates high

lateral resolution up to several microns. However, for the visible and NIR photons, the scattering

coefficient μ_s is quite large in soft tissue, typically over $100 \ cm^{-1}$. Even though the scattered

photons can retain their original forward trajectory mostly with a dimensionless anisotropy

$g{\sim}0.9$ (Steven 2013), the effective scattering coefficient $\mu_s' = \mu_s(1 - g)$ only permits a transport mean free path $1/\mu_s'$ of about $1\ mm$, which binds the penetration depth of the optically focused microscopy. The lateral resolution of an acoustic-focused microscope highly depends on the design of the focused transducer, but it is generally worse than its axial resolution.
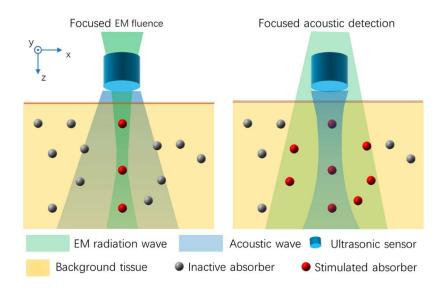
Figure 2-2. Schematic of focusing strategies in scanning microscopy.

No matter which type of focusing methods is applied, the problem of acoustic wave detection can be simplified to 1D near its focal zone (Xu and Wang 2006). Considering the depth-variant sensitivity of the detection sensor, the received time-resolved pressure $p(t)$ should be:

$$p(t) \propto \frac{1}{2}p_0(z)h_s(z) = \frac{1}{2}\Gamma(z)H_d(z)h_s(z)|_{z=tv_s} \qquad 2\text{-}19$$

In actual 1D scenario, the initial pressure p_0 will induce two TA waves, which travel in the $+z$ and $-z$ directions with one-half the amplitude. So, in this simplified 1D model, a directly proportional sign is used in the equation. Through a B-scan in the x direction perpendicular to

the tissue surface, a 2D TA microscopic image $I(x, z)$ for the sample's cross-section can be formed.

2.2.2 Computed tomography

As a full-fledged imaging method, TA computed tomography can be achieved with a 1D/2D ultrasonic sensor array or its scanning equivalents. Ideally, each element will receive acoustic waves from a large acceptance angle. The acquired acoustic wave pressure $p(t)$ measured from a single sensor element cannot translate to initial pressure directly. Reconstruction based on the signals acquired from all distributed sensor elements is necessary. Under the assumption that the medium is acoustically lossless and homogeneous, universal back-projection could be applied to reconstruct the distribution of initial pressure $p_0(r)$ by (Xu and Wang 2005):

$$I(\boldsymbol{r}) = p_0{}^b(\boldsymbol{r}) = \int_{\Omega_0} \frac{d\Omega_0}{\Omega_0} 2 \left[p(\boldsymbol{r}_0, t) - t \frac{\partial p(\boldsymbol{r}_0, t)}{\partial t} \right] \Bigg|_{t = \frac{|\boldsymbol{r} - \boldsymbol{r}_0|}{v_s}} \qquad \text{2-20}$$

where $d\Omega_0$ is the solid angle of the detection element located at $\boldsymbol{r}_0$ with respect to a reconstruction point at $\boldsymbol{r}$. The term $d\Omega_0/\Omega_0$ is a weighting factor that considers the effective area of signal element detection according to the whole detection surface of the array. If the chosen medium has highly acoustic heterogeneities, then a time-reversal method could be applied (Treeby and Cox 2010), whereby the wave equation will be numerically solved and back-propagated from detection locations into the medium in a time-reversed order. Since the induced acoustic wave propagates in all three dimensions, a spherical 2D array-based imaging strategy was originally required for accurate reconstruction. In 2D circular computed tomography (circular 1D-array), the radial and tangential resolutions will depend on the frequency bandwidth of the acoustic sensor, while the elevational direction will not be well

18

confined unless a focusing technique, such as cylindrical acoustic focusing, is applied in each element. A 1D linear array will encounter the problem of decaying lateral resolution in a deep field.

2.3 Inverse Problems in Quantitative TA Images

As described above, either TA scanning microscopy or computed tomography aims to form image $I(\mathbf{r})$ based on the acquired time-resolved acoustic pressure $p(\mathbf{r_0}, t)$. An accurate reconstruction algorithm, which forms an image $I(\mathbf{r})$ directly proportional to initial pressure $p_0(\mathbf{r})$, can be applied to solve the first inverse problem and show some bio information in the region of interest. However, further quantitative interpretation may be required to reveal specific tissue properties, characterize tissue status, or indirectly detect radiation excitation. Mostly, these applications can be achieved by solving more inverse problems according to the mechanisms described above. As described in eq. (2-18), the heat absorption rate $H(\mathbf{r}, t)$ can be calculated from the distribution of initial pressure $p_0(\mathbf{r})$, if the distribution of Grüneisen parameter $\Gamma(\mathbf{r})$ is known or can be assumed to be uniform. In the case of monitoring dose delivery by x-ray beam, the temporal dose density D_r can be calculated from $H(\mathbf{r}, t)$ through eq. (2-4). To evaluate chemical components based on radiation absorption, the spatial absorption coefficient $\mu_a(\mathbf{r})$ cannot be resolved based on $H(\mathbf{r}, t)$, as the unknown radiation fluence rate $\Phi(\mathbf{r}, t)$ is highly dependent on $\mu_a(\mathbf{r})$ and the scattering coefficient $\mu_s(\mathbf{r})$ following eq. (2-1). At once, the spatial absorption coefficient at multiwavelength $\mu_a(\mathbf{r}, \lambda)$ can be determined, and the chemical concentration $c_i(\mathbf{r})$ can be resolved based on the equation:

$$\mu_a(\boldsymbol{r}, \lambda) = \sum_i c_i(\boldsymbol{r})\, a_i(\lambda) \qquad\qquad\qquad \text{2-21}$$

where $a_i(\lambda)$ is the known absorption of chemical component i under the radiation of wavelength λ. The flow of the inverse problems in the quantitative TAI discussed above is plotted in Figure 2-3.
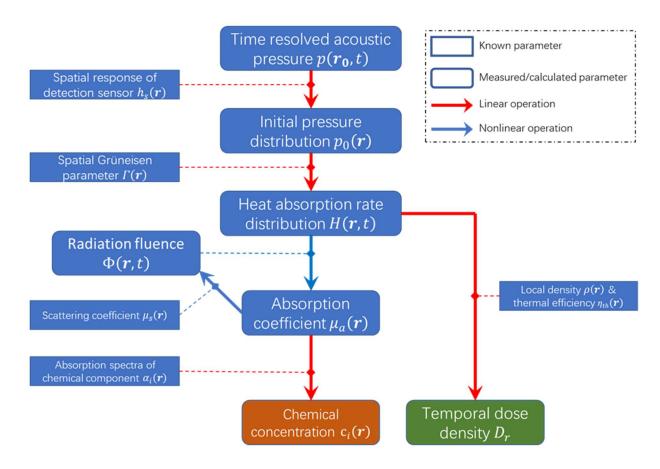
Figure 2-3. Frame of inverse problems in quantitative TAI for solving chemical concentrations and temporal dose density.

2.4 Summary

In this chapter, the forward problems, from radiation excitation to acoustic wave generation, were presented and formulated. The mechanisms behind radiation energy delivery, heat transfer,

and acoustic wave generation were introduced. The imaging strategies and reconstruction methods for TA scanning microscopy and computed tomography were also introduced. The flow of inverse problems in quantitative TAI was discussed. The work introduced in the following chapters, including quantifying relevant histochemical components in tissue with PAI and monitoring dose delivery during radiation therapy with XA imaging, are used to solve the inverse problems under this frame.

Chapter 3

Characterizing Intestinal Inflammation and Fibrosis in Crohn's Disease by Photoacoustic Microscopy

In the following two chapters, a laser-based thermoacoustic imaging (TAI) implementation, photoacoustic microscopy, is proposed to improve Crohn's disease diagnosis through the characterization of inflammation and fibrosis in intestinal strictures. The term *photoacoustic* is used instead of *thermoacoustic* to specify the radiation excitation source applied. The terms *light* and *photon* are used to describe the EM wave and its particle belonging to the region of the spectrum from UV to NIR if there is no other specific explanation.

3.1 Introduction

Crohn's disease (CD) is a type of inflammatory bowel disease affecting 700,000 people in the United States (Cohen, Larson et al. 2000, Loftus, Schoenfeld et al. 2002, Lawrance, Welman et al. 2009). It starts from intermittent segmental intestinal inflammation and proceeds to cumulative, irreversible intestinal fibrosis, along with the progressive thickening of the bowel wall (Stidham and Higgins 2016). The pathology of CD is characterized by obstructing intestinal strictures due to inflammation, fibrosis, or a combination of both (Oberhuber, Stangl et al. 2000, Lichtenstein, Olson et al. 2006). Inflammatory strictures are usually medically treated, while fibrotic strictures are irreversible and may have to be removed surgically. Seventy percent of

22

Crohn's patients require at least one surgery (Cohen, Larson et al. 2000), while 13% have an unremitting disease and 10% experience prolonged remission (Loftus, Schoenfeld et al. 2002). The accurate characterization of the intestinal strictures, especially the quantification of the relative contribution of fibrosis and inflammation, is therefore critical for the management of CD (Domènech, Mañosa et al. 2009, Jones and Finlayson 2010, Stidham and Higgins 2016).

The standard assessment of CD strictures is largely achieved via extrapolation from superficial biopsies (Achkar, Carey et al. 1986, Dandalides, Carey et al. 1989), in which an endoscope with a light source and camera is inserted into the digestive tract. By observing video feedback from the camera, clinicians first localize the strictures in the intestinal tract. Then, small sample pieces are removed from the inner layer of the strictures for histopathology. These mucosal biopsies are helpful in identifying the inflammatory condition through corresponding hemoglobin-dependent tissue perfusion. However, due to the limited depth of the endoscopic biopsy procedure, mucosal biopsies rarely reach the deeper layers, where fibrosis, with collagen as a major component, develops (Graham, Diegelmann et al. 1988). Moreover, as the number of sampling locations is limited during an endoscopic biopsy procedure, the comprehensive evaluation of intestinal strictures is hard to achieve (Graham, Diegelmann et al. 1988, Tarján, Tóth et al. 2000, Paolantonio, Ferrari et al. 2009).

Conventional imaging technologies, including ultrasound (US) imaging (Tarján, Tóth et al. 2000), computed tomography (CT) (Oberhuber, Stangl et al. 2000, Boudiaf, Soyer et al. 2001, Lichtenstein, Olson et al. 2006), and magnetic resonance imaging (MRI) (Lawrance, Welman et al. 2009, Paolantonio, Ferrari et al. 2009), have been used to identify fibrotic intestinal strictures by imaging the stratified architecture in the strictures. However, their diagnostic accuracy is limited, as these modalities cannot assess intestinal strictures at the molecular level.

The distinctive optical properties of collagen and hemoglobin (shown in Figure 2-1) have prompted the use of optical imaging approaches, such as diffuse optical spectroscopy (DOS) (Richards-Kortum and Sevick-Muraca 1996, Messmann, Endlicher et al. 2003) and optical coherent tomography (OCT) (Shen, Zuccaro Jr et al. 2004, Yang, Tang et al. 2005), to assess fibrosis and inflammation conditions. However, DOS can only evaluate the molecular components of the bowel wall; it cannot yield sufficient spatial information. Backscattering-based OCT, which has excellent spatial resolution, can only image detailed bowel wall structures at a limited depth (~1 mm) and cannot interrogate their molecular components. Considering the demand for both high optical sensitivity and high spatial resolution, photoacoustic microscopy (PAM) could therefore represent a potentially valuable tool for characterizing diseased conditions in intestinal strictures. The stratified tissue architecture in the bowel wall is on the order of tens of microns and is millimeters beyond the stricture's inner surface (Stidham, Xu et al. 2011, Chiorean, Schreiber-Dietrich et al. 2014), which is ideally covered by acoustic resolution PAM (AR-PAM).

In this chapter, to validate the feasibility of assessing the spatially varying molecular components in the intestinal strictures of Crohn's disease with AR-PAM, a prototype AR-PAM system, which is developed and applied to image human intestinal specimens at multiwavelengths *ex vivo,* is discussed. The non-uniform fluence distribution of light and spatial sensitivity of the US transducer is also compensated for. The PA molecular component images showing the concentration distributions of the molecular components are obtained based on acquired multiwavelength PA intensity images. The results are discussed and compared with histology images.

3.2 Experimental Setup

The schematics of the AR-PAM system are shown in Figure 3-1. A tunable optical parametric oscillator (OPO) laser (Vibrant B, OPOtek Inc., Carlsbad, CA, USA) pumped by the second harmonic output of an Nd:YAG pulsed laser (Brilliant B, Quantel, Bozeman, MT, USA) provided the illumination laser for the AR-PAM. A tunable range of $680 \, nm \sim 950 \, nm$ and $1200 \, nm \sim 2440 \, nm$, besides the pumping wavelengths of 532 nm and 1064 nm, can be provided by the combined laser system. The output beam of the laser was collimated with two plano-convex lenses (Lens 1: $f = 6cm$, Lens 2: $f = 1cm$) and coupled into a bundle of nine multimode optical fibers (0.39 NA, $400 \, \mu m$ core, Thorlabs). One spherically focused transducer (48-MHz central frequency, 30% bandwidth, 3.1-mm focal length, 3.5-mm aperture) received the acoustic signals. The transducer and the output ends of the optical fibers were securely fixed by a cone-shaped holder, which allowed for the adjustment of the directions of the fiber tips for optimal illumination. The optical fibers were evenly distributed in a circle to formulate a broad illumination pattern, reducing PA signal intensity at the tissue surface and guaranteeing enough light penetration in deep tissue for a narrower signal dynamic range. The optical density on the tissue surface was maintained below the ANSI safety limit for all wavelengths, at approximately $16 \, mJ/cm^2$. The cone-shaped holder was precisely driven by a 3D linear translation stage for a 2D/3D raster scan. The PA signals were filtered by a high-pass filter and amplified by 40 dB with a low-noise amplifier before being recorded by an 8-bit digitizer card (DP1400, Agilent Tech, USA).
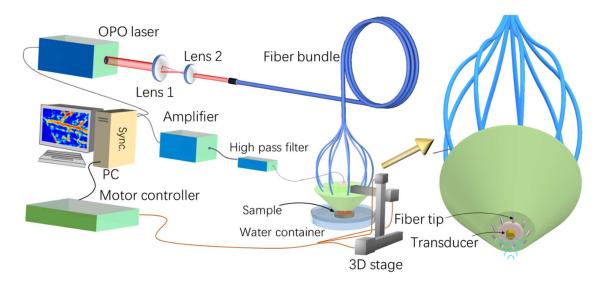
Figure 3-1. Schematics of the AR-PAM system.

The US transducer applied in the AR-PAM system was selected for its high frequency properties. The axial resolution and lateral resolution of the focusing transducer can be precisely estimated by (Wang and Hu 2012):

$$R_{axial} = 0.88 \frac{v_s}{f_h} \qquad \text{3-1}$$

$$R_{lateral} = 0.71 \frac{v_s}{f_c \cdot NA} \qquad \text{3-2}$$

where f_h is the high bound of the transducer frequency response, f_c is the central frequency, and NA is the numerical aperture. In this case, the axial resolution R_{axial} is about 22 microns and the lateral resolution is about 37 microns. However, due to the high attenuation of acoustic waves at high frequency, which is 0.5 dB/cm-MHz in soft tissue (Foster, Lockwood et al. 1993), the axial resolution suffers a significant decay at a deep region. The actual spatial resolution of the system was tested with a 46 AWG (40 μm in diameter) nickel wire, which was submerged in a 1% intralipid water solution (tissue equivalent light-scattering medium) (Lai, Xu et al.

2014). The axial and lateral resolutions were acquired near a focal depth of $49\ \mu m$ and $65\ \mu m$, respectively.

Before performing scans, the samples were cut into pieces of around 15 mm by 15 mm and fixed in a petri dish using porcine gel (10% in weight) with the inner surface facing up. A small amount of water was added on top of the samples for acoustic coupling. B-scans perpendicular to the tissue surface with a step size of $50\ \mu m$ were performed to form 2D PA images of the cross-sections of the samples at selected wavelengths. For each sampling location, PA signals were averaged 10 times to improve the signal-to-noise ratio (SNR).

3.3 Obtaining PA Molecular Component Images

As shown in Figure 2-1, the optical absorption spectra of collagen and hemoglobin are distinctive. The hemoglobin in tissue is usually characterized using light in the visible spectrum, while collagen can be detected within a range of wavelengths at around 1300 nm. However, considering that lipids (commonly observed in human specimens) also have strong absorption near 1300 nm, one more wavelength should be added to separate collagen from lipids. In this study, a wavelength combination of 532 nm, 1220 nm, and 1310 nm was employed. The wavelength of 532 nm was selected not only for its strong optical absorption of hemoglobin but also for the similar absorption coefficients of oxy- and deoxygenated hemoglobin, which minimize the differences between *ex vivo* and *in vivo* measurements caused by varied oxygenation levels. The wavelength of 1310 nm was chosen for its relatively high optical absorption by collagen and lower optical absorption by lipids. The wavelength of 1220 nm was selected for its ability to separate clustered lipid depositions from collagen. The absorption coefficients at each wavelength for different materials are listed in Table 3-1 below (Cheong,

Prahl et al. 1990, Wang, Chai et al. 2011, Tian, Xie et al. 2015). Even though water has a strong

optical absorption in the NIR range and contributes most of the attenuation for the cases of 1310

nm and 1220 nm, it is not necessary to investigate the water component since no correlation has

been discovered between diseased conditions and water content variation (Kim, Johnson et al.

2008, Stidham, Xu et al. 2011). Also, considering that water is widely distributed inside tissue,

the contribution from water to total optical absorption can safely be considered as a background,

an assumption which will be further discussed in Section 3.3.2.

Table 3-1. Specific absorption coefficients

Wavelength:	Hemoglobin	Collagen	Lipid	Water
532 nm	$103.46\ cm^{-1}$	$0.5694\ cm^{-1}$	$0.0120\ cm^{-1}$	$0.0003\ cm^{-1}$
1220 nm	$0.2647\ cm^{-1}$	$0.3434\ cm^{-1}$	$1.6460\ cm^{-1}$	$0.9543\ cm^{-1}$
1310 nm	$0.1307\ cm^{-1}$	$0.2247\ cm^{-1}$	$0.0741\ cm^{-1}$	$1.2361\ cm^{-1}$

As the goal was to generate a PA molecular component image that would show the

distribution of specific chemical components $c_i(\mathbf{r})$, the inverse problems mentioned in Section

3.2 should be solved step by step.

3.3.1 Compensation for the spatial sensitivity of the US transducer

According to eq. (2-19), the A-scan signal acquired by $p_{x_i}(t)$ at scanning position x_i

through the AR-PAM system can be related to initial pressure $p_{0,x_i}(z)$ by compensating for the

spatial sensitivity of the ultrasonic sensor $h_s(z)$:

$$p_{0,x_i}(z) = p_{x_i}(t)/h_s(z)\big|_{t=z/v_s} \hspace{2cm} 3\text{-}3$$

The ultrasound beam pattern for the applied transducer was simulated by the FOCUS software package (https://www.egr.msu.edu/~fultras-web/) and shown in Figure 3-2 (A), which considered its central frequency at 48 MHz and with a bandwidth of 30 MHz. The acoustic attenuation was estimated as in the case of typical soft tissues with 0.5 dB/cm-MHz. The 1D spatial sensitivity of the transducer $h_s(z)$ was calculated based on the simulated beam pattern and shown in Figure 3-2 (B), which assumed that the transducer only received a signal from the effective region around the transducer-focusing axis with a diameter of 50 µm, as illustrated by the red color in Figure 3-2 (C).
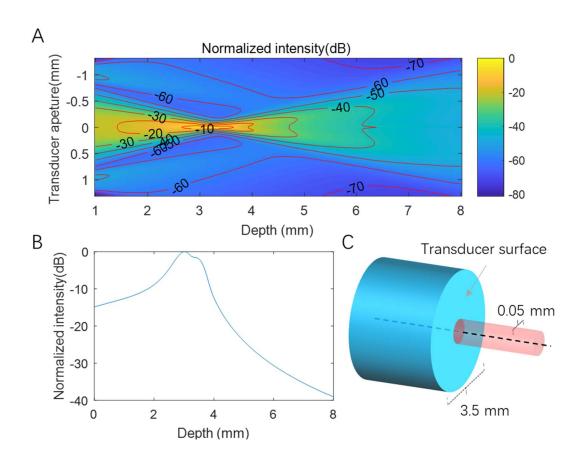
Figure 3-2. (A) Simulated ultrasound beam pattern. (B) 1D spatial sensitivity of the transducer. (C) Illustration of the effective acquisition region.

3.3.2 Compensation for the light fluence distribution

According to the RTE (eq. [2-1]) introduced in Section 2.1.1, the light fluence rate $\Phi(r, t)$ does not have a simple analytical solution. For the numerical solutions based on the finite element method (Tarvainen, Vauhkonen et al. 2006) or Monte Carlo method (Wang, Jacques et al. 1995), the knowledge of $\mu_a(r)$ and $\mu_s(r)$ is also required. To solve this nonlinear problem, the sample tissues were assumed to be homogeneous media so that the distributions of the targeted chemical components could be treated as perturbations (Cox, Laufer et al. 2012). Therefore, the spatial absorption coefficient $\mu_a(r)$ can be separated as:

$$\mu_a(r) = \mu_a{}^{(0)} + \mu_a{}^{(1)}(r) \qquad\qquad 3\text{-}4$$

where $\mu_a{}^{(0)}$ is the absorption coefficient for the homogeneous background, and $\mu_a{}^{(1)}(r)$ is the spatial absorption coefficient due to the perturbation, and is much smaller compared to $\mu_a{}^{(0)}$. The spatial scattering coefficient could also be expressed in a similar form. Here, it can be approximated that light fluence changes due to perturbation can be ignored. The light fluence rate in further calculations will stay as $\Phi^{(0)}(r, t)$, which is the fluence distribution caused by $\mu_a{}^{(0)}$ and $\mu_s{}^{(0)}$. So, the heat absorption rate $H(r, t)$ becomes:

$$H(r, t) \approx \left(\mu_a{}^{(0)} + \mu_a{}^{(1)}(r)\right) \Phi^{(0)}(r, t). \qquad\qquad 3\text{-}5$$

Since the pulse duration of the applied light source in this study (several nanoseconds) is shorter than the time period resolvable by the ultrasound transducer ($\sim \frac{1}{50MHz} = 20ns$), the temporal profile $h_t(t)$ of the light source can be treated as a Dirac Delta function, eq. (2-17) can be rewritten as (Zhou, Yao et al. 2016):

$$p(t) = \frac{1}{4\pi v_s^2} \frac{\partial}{\partial t} \int d\boldsymbol{r} \frac{1}{r} p_0(\boldsymbol{r}) h_s(\boldsymbol{r}) \delta\left(t - \frac{r}{v_s}\right).$$ 3-6

The time derivative inside the equation functions as a ramp filter, suppressing the low-frequency components in the acquired signal contributed by the term $\mu_a{}^{(0)}$. Therefore, taking the light fluence during the short laser pulse as $\Phi_p(\boldsymbol{r}) = \int_0^{\tau_p} \Phi^{(0)}(\boldsymbol{r}, t) dt$, the filtered absorption distribution $\mu_{a,f}{}^{(1)}(z)$ can be calculated from initial pressure $p_{0,x_i}(z)$ by:

$$\mu_{a,f}{}^{(1)}(z) = \frac{p_{0,x_i}(z)}{\Gamma(z)\Phi_p(z)}.$$ 3-7

As the pulse duration τ_p is spatially invariant and fixed during all measurements, it was dropped during calculations.

In this study, Monte Carlo simulations (Wang, Jacques et al. 1995) were performed for each wavelength to estimate $\Phi_p(\boldsymbol{r})$ inside the sample tissues. The background optical properties were calculated based on the specific absorption coefficients listed in Table 3-1 with the estimated concentrations of water, lipids, and hemoglobin at 70%, 25%, and 0.05%, respectively, and the scattering properties were calculated following the approach in (Steven 2013). A low hemoglobin concentration was assumed due to the loss of blood during surgical sample collection. The optical properties applied in Monte Carlo simulations are shown in Table 3-2 below. Using the estimated beam profile at the sample surface shown in Figure 3-3 (A), fluence distributions for the wavelengths of 532 nm, 1220 nm, and 1310 nm were simulated and shown in Figure 3-3 (B) to (D), respectively. The light fluence distribution along the transducer-focusing axis $\Phi_p(z)$ is shown in Figure 3-3 (E).

Table 3-2. Optical parameters in Monte Carlo simulations

Wavelength	Absorption Coefficient μ_a	Reduced Scattering Coefficient μ_s'	Scattering Anisotropy g
532 nm	$0.07\ cm^{-1}$	$15.3\ cm^{-1}$	0.95
1220 nm	$1.29\ cm^{-1}$	$5.5\ cm^{-1}$	0.95
1310 nm	$1.09\ cm^{-1}$	$5.0\ cm^{-1}$	0.95
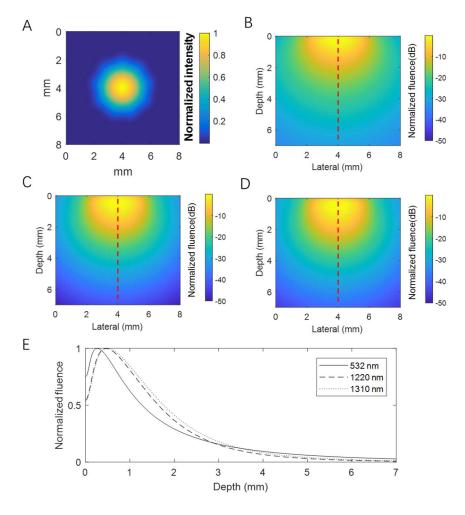
Figure 3-3. (A) Estimated beam profile on the surface of the sample. (B) Monte Carlo-simulated 2D light fluence distribution in the plane, including the transducer-focusing axis at a wavelength of 532 nm. (C) at 1220 nm. (D) at 1310 nm. (E) Light fluence distribution along the transducer-focusing axis (red dashed lines in B-D).

3.3.3 Relative concentration calculation

Noting that the Grüneisen parameter $\Gamma(r)$ is not a constant and is strongly different in water and lipid-based mediums (Tian, Xie et al. 2015), the absorption distribution may not be resolved directly from eq. (3-7). To simplify this problem, the Grüneisen parameters in all regions were considered to be the same (include hemoglobin and collagen locations), except in the lipid location. By assuming the Grüneisen parameter $\Gamma(r)$ to be 1 everywhere in tissue, the PA molecular component image showing the relative concentration of each molecular component rather than its actual or absolute value could be resolved by inversing eq. (2-21):

$$\begin{bmatrix} c_{hb} \\ c_{cg} \\ c_{lp} \end{bmatrix} = \begin{bmatrix} a_{hb5} & a_{cg532} & a_{lp532} \\ a_{hb1220} & a_{cg1220} & a_{lp1220} \\ a_{hb1310} & a_{cg1310} & a_{lp1310} \end{bmatrix}^{-1} \times \begin{bmatrix} \mu_{532} \\ \mu_{1220} \\ \mu_{1310} \end{bmatrix} \qquad \text{3-8}$$

where *hb* is hemoglobin, *cg* is collagen, and *lp* is lipid. In this case, the calculated relative concentrations will contain different contributions from the specific Grüneisen parameters for each chemical component.

3.4 Experimental Results and Discussion

Surgically removed de-identified human intestinal strictures, which were procured through the standard procurement procedures in the Department of Surgery, were scanned with the prototype AR-PAM system. The specimens were prepared following the procedures mentioned in Section 3.2 and scanned with a step size of $50\ \mu m$ and 140 steps to form 2D PA images of the cross-sections of the samples at wavelengths of 532, 1220, and 1310 nm. The total scanning time for each specimen was about 15 minutes and was limited by the 10-Hz repetition rate of the

laser source. After scanning, the scanned portions of the specimens were cut off for histology with Hematoxylin and eosin (H&E) and Masson's trichrome staining. The acquired PA images were processed as in previous sections, and pseudo-color PA molecular component images showing relative concentrations of hemoglobin, collagen, and lipids were formed.

3.4.1 Results

The raw 2D PA images (envelope detected) acquired at three wavelengths from one of the samples are shown in Figure 3-4 (A). The spatial sensitivity of the US transducer and the light fluence distribution were considered to obtain the compensated images shown in Figure 3-4 (B). The relative concentrations were calculated and displayed in PA molecular component images in Figure 3-4 (C), where the relative concentrations of hemoglobin, lipids, and collagen are shown in red, blue, and green, respectively.

Figure 3-5 (A) and (C) show the pseudo-color PA molecular component images for two representative human intestinal stricture specimens (#4 and #5), respectively. The color scales were normalized to the maximum concentration of hemoglobin. Both samples had collagen components, which were confirmed in (B) and (D) with Masson's trichrome staining. The inflammations in the samples were confirmed by H&E staining, as shown in the insertions in (B) and (D), in red boxes with 20x magnification. Spatial correlations between the histology and the PA images are marked by green arrows (high collagen concentration), red arrows and dashed contours (neovasculature-containing hemoglobin), and blue arrows (lipid deposition caused by edema). The porcine gel for fixing the samples with a low collagen concentration was also stained in blue, yet with a uniform texture, and marked by black arrows. The curvatures of the samples were distorted because of histology-related cutting. Therefore, a perfect alignment

34

between the histology photos and the PA molecular component images could hardly be achieved. However, the stratified architecture of the samples was resolved, and spatial correlations can still be identified.
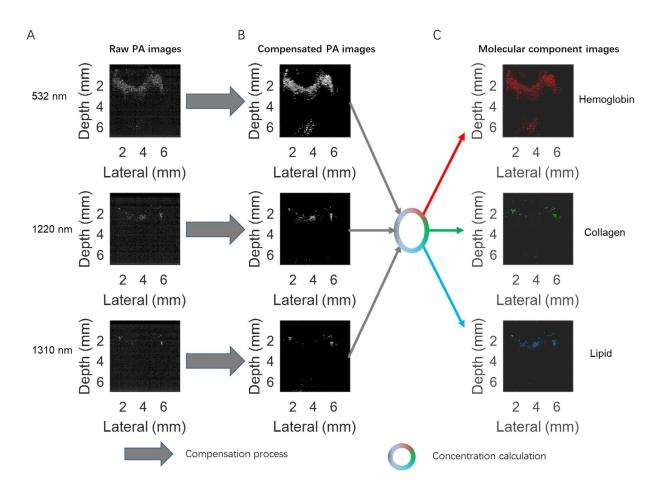
Figure 3-4. Illustration of the image processing procedure.
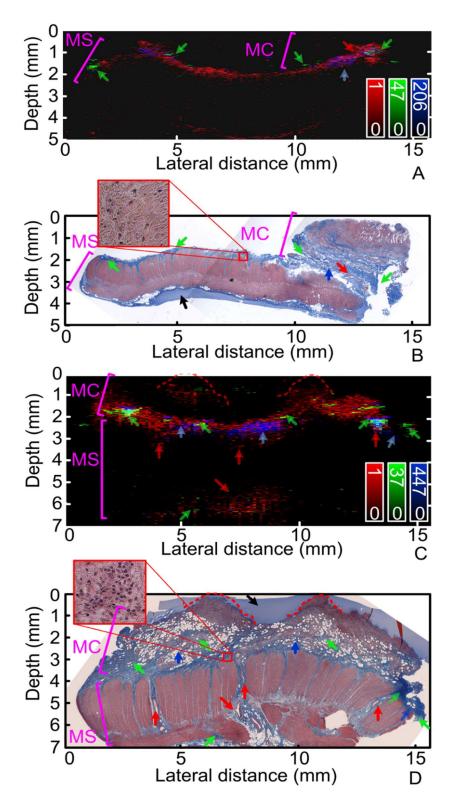
Figure 3-5. Representative PA molecular component images (A) (C) and histology images (B) (D) of human intestinal strictures. MC: mucosal layer; MS: muscle layer.

3.4.2 Discussion

The compensation for light fluence distribution at each wavelength was based on the homogeneous-perturbation assumption. Collagen content, although possessing the lowest distinctive optical absorption spectrum among the three molecular components studied, was detected at a depth of 6.5 mm (Figure 3-5 [C]). Noting that water contributes the most absorption at the NIR wavelength range, its concentration should not change when any other components are increased. Any kinds of chemical components, not only collagen, may contribute a negative contrast due to lower absorption compared with the excluded water and should bring a negative contribution to $\mu_a{}^{(1)}(\boldsymbol{r})$. Currently, the methods applied to analyze the detected acoustic wave pulse, such as envelope detection, are not sensitive to the phase, which means that this kind of situation can hardly be identified directly. Meanwhile, the assumption of a homogeneous background may not be appropriate when an extremely high concentration of hemoglobin appears and cannot be treated as one of the perturbations. In this case, iterative methods (Cox, Arridge et al. 2006, Cox, Laufer et al. 2012) that calibrate the optical fluence distribution within the tissue samples may become necessary. The generated relative concentrations of lipids in Figure 3-5 appeared to be extremely strong but did not break the homogeneous-perturbation assumption, because the Grüneisen parameter of lipids is about 20 times larger than water at room temperature (Tian, Xie et al. 2015) and is combined with the relative concentration during the calculation.

The mucosal layer and the top of the muscle layer of primary diagnostic interest are adequately covered by the focal zone of the transducer, while the PA signals from deep tissues are compensated for by the simulated spatial sensitivity of the US transducer. However, the large NA and limited focal length of the transducer employed in this AR-PAM system make it difficult

to obtain any high-quality signal from regions deeper than 4 mm, where the SNR drops by at least 40 dB due to decreased signal strength. Moreover, directional confinement due to the acoustic focusing of the transducer to guarantee the 1D A-scan following eq. (2-19) becomes weak for depths outside the focal zone. In this AR-PAM system, even though the 3D translation stage can achieve multiple B-scans at different distances from the tissue surface, the maximum depth is still limited by the focal length of the transducer. Therefore, a transducer with a larger focal length and relatively large NA (5.2-mm focal length, 3.5-mm aperture) should be used as an alternative for examining human intestinal strictures in the future.

3.5 Summary and Conclusion

In this chapter, a prototype AR-PAM system developed to assess the spatially varying molecular components in intestinal strictures of Crohn's disease was outlined. A method for generating PA molecular component images based on multiwavelength PA intensity images acquired by AR-PAM was proposed, considering the non-uniform fluence distribution of light in tissue and the spatial sensitivity of the US transducer. The imaging results for *ex vivo* tissues from human subjects showed the concentration maps of relevant molecular components, which can be spatially correlated with histology images. The developed prototype AR-PAM system has verified the capacity to non-invasively produce molecular component images in *ex vivo* human intestinal strictures through superficial measurements. This suggested AR-PAM can be a potential tool for the diagnosis of the diseased conditions in intestinal strictures.

Chapter 4

Characterizing Intestinal Strictures of Crohn's Disease by Endoscopic Photoacoustic Imaging

4.1 Introduction

The ultimate goal of applying photoacoustic (PA) imaging technique in Crohn's disease diagnosis is to non-invasively, accurately characterize intestinal strictures in clinic situations. Due to the conflict between the demands of high spatial resolution and the limitations of imaging depth, an endoscopic version of acoustic resolution PA microscopy (AR-PAM) that can be implemented with a clinical endoscope during a diagnostic procedure is required. In the previous chapter, the small, spherically focused transducer ensured a desirable resolution for observing histological features and offered a direction for further miniaturization of AR-PAM in the form of an endoscopic imaging probe.

Recently, several PA endoscopy (PAE) systems have been developed (Yang, Chen et al. 2012, Yang, Favazza et al. 2012, Li, Yang et al. 2014, Yang, Li et al. 2014, Yang, Favazza et al. 2015). The capability and feasibility of their clinical applications in gastrointestinal (GI) imaging (Yang, Li et al. 2014) and urogenital disease diagnosis (Li, Yang et al. 2014) were investigated with tissue-equivalent phantoms and *ex vivo* tissues. Their circular scanning feature, which images the cross-section of the cylindrical probe, is not applicable in the inner lumen of the bowel with a dimension larger than the scanning probe. Due to circular scanning, the nonlinear

sampling strategy in their sector image limits the spatial resolution at a deep field of the image. Therefore, a longitudinal image scanning strategy was preferred to meet the requirements for quantifying histochemical components and their distributions inside the strictures. Given that capsulated devices are widely used in endoscopy (Qureshi 2004, Eliakim, Fireman et al. 2006), a miniaturized AR-PAM system was developed into a prototype capsule-shaped side-view PA probe that can be attached to the inner surface of the bowel wall for longitudinal image scanning.

In this chapter, a prototype capsule-shaped side-view scanning PA imaging probe that miniaturizes the scanning head of AR-PAM is described. Motion artifacts caused by intestinal peristalsis in *in vivo* scenarios were compensated for to improve image quality. A digital refocusing method was applied to overcome the problem of decayed lateral resolution outside the focal zone of the focusing transducer. The trinitrobenzene sulfonic acid (TNBS) rabbit model of intestinal inflammation and fibrosis was employed to perform *in vivo* colonoscopy with the prototype probe. The quantitative imaging results were statistically analyzed and found to be consistent with the histopathology analysis.

4.2 Capsule-shaped AR-PAM Probe and Peripheral System

Figure 4-1 (A) shows the schematic diagram of the prototype capsule-shaped AR-PAM probe, including the acquisition system. The probe consists of a capsule shell with a side-viewing window and a translation stage fabricated using a 3D printer with VisiJet M3 Crystal (ProJet 3500, 3D System, Rock Hill, SC, USA). A spherically focused transducer (50-MHz central frequency, 80% bandwidth, 3.2-mm focal length, 2-mm aperture) and multimode optical fiber (0.39 NA, $600 \, \mu m$ core, Thorlabs, Newton, NJ, USA) were fixed in the translation stage

(Figure 4-1 [B]). As shown in Figure 4-1 (C), the tip of the optical fiber was placed in the stage

with an 8°-tilted angle so that the delivered light would be reflected by the optical prism

($1.5\ mm \times 1.5mm \times 1mm$, Tower Optical Corporation, Boynton Beach, FL, USA) and

projected through the side-viewing window. Figure 4-1 (D) displays the calculated beam pattern

projected onto the bowel wall covering the focusing direction of the transducer with its center.

The translation stage was attached to a compression spring (94125K414, McMaster-Carr,

Elmhurst, IL, USA) and driven by an external step motor through a pulling string. The side-

viewing window was sealed with a polyethylene (PE) membrane with a thickness of $12.7\ \mu m$,

and the probe shell was filled with deionized water for optical transmission and acoustic

coupling.

During the scanning, the side-viewing window contacted the surface of the imaging volume,

and the PA measurements were acquired over a longitudinal range of 4 mm at the step of

$50\ \mu m$. A tunable (680 nm ~ 1700 nm) optical parametric oscillator (OPO) laser (VibrantB,

Opotek Inc., Carlsbad, CA, USA) pumped by the second harmonic output of a Nd:YAG pulsed

laser (Brilliant B, Quantel, Bozeman, MT, USA) was used as the illumination source. An optical

energy of $1.5\ mJ$ per pulse at a 10-Hz pulse repetition rate was coupled to the optical fibers in

the probe, forming an optical energy density of approximately $7\ mJ/cm^2$ at the scanning

surface (estimated based on the calculated beam pattern). The energy level was below the safety

limit of $20\ mJ/cm^2$ established by American National Standard Institute (ANSI). The PA

signal was amplified by 40 dB with a low noise pre-amplifier and recorded by a 14-bit digitizer

card (200 MHz, GaGe, DynamicSignals LLC, Lockport, IL, USA) in the PC. For each scanning

step or sampling location, PA signals were averaged 30 times to improve signal-to-noise ratio (SNR).
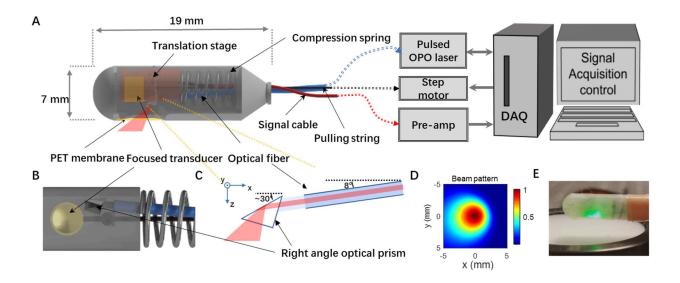
Figure 4-1. (A) Schematic diagram for the prototype capsule-shaped AR-PAM probe, including the acquisition system. (B) Bottom view of the translation stage without the capsule shell. (C) Illustration of the light path through the optical prism. (D) Calculated beam pattern projected onto the bowel wall. (E) Photograph of the probe.

4.3 Imaging Method

4.3.1 Motion artifact removal

As shown in Figure 4-2, because of intestinal peristalsis *in vivo*, the distance between the transducer and the tissue surface may have been slightly displaced, which could have in turn led to the time delay variations that appeared in the signals and induced phase mismatches of approximately 20 ns (corresponding to 30 μm) among the measurements. The motions of the bowel wall presented two problems: incoherent signals for averaging, and discontinuity in B-scan images.
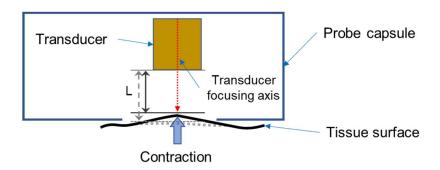
Figure 4-2. Schematic of signal displacement due to contraction in peristalsis.

Due to phase mismatches among the 30 repetitive measurements taken at a single scanning step, the following averaging process decreased the SNR (shown in Figure 4-3 [A] and [B], respectively). To suppress this kind of artifact and maintain the SNR, a phase correlation based on least-square estimation was applied to the 30 raw signals to compensate for the delay variations and improve the SNR (shown in Figure 4-3 [C] and [D]).
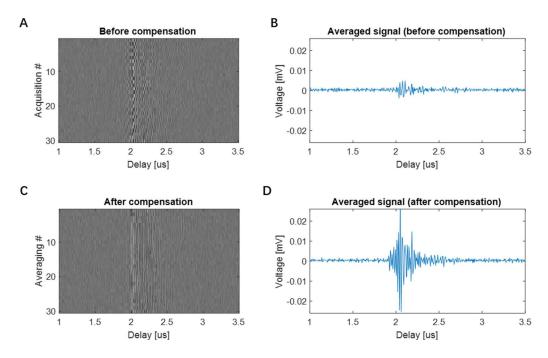
Figure 4-3. (A) Acquired raw signals at the signal step before taking the average. (B) A-scan signal averaged from (A). (C) Delay-compensated signals after data in (A) were applied to phase correlation. (D) A-scan signal averaged from (C).

Comparing to the period of repetitive measurements at each step with 30 averaging, the whole scanning process took much more time and was more vulnerable to motion. In the B-scan PA images, the misalignment between the signals at different acquisition locations manifested as feature discontinuities and could not be compensated for through phase correlation directly. Fortunately, a strong US echo was generated as the laser scattered to the transducer surface and reflected from the tissue surface. Delay compensation could therefore be performed based on the variations that occurred for this US echo. Figure 4-4 (A) displays an example of an A-scan signal that contains a PA signal peak and a US echo peak, while the schematic figure of the travel paths of different signals is shown in Figure 4-4 (B).
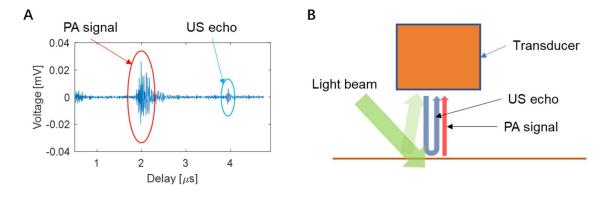
Figure 4-4. (A) A-scan signal with PA signal and US echo; (B) schematics of US echo path and PA path.

The US echo usually manifests as a clear peak and can be correlated with the adjacent measurements in a straightforward way, such that the delay compensation for US echo alignment is much simpler. Since the travel paths of the US echo (round-trip) and PA signal (one-way) are different, a factor of 0.5 was applied in the delay compensation to align the PA signals. Figure 4-5 shows an example of the alignment achieved for PA signals across 80 acquisition locations based on US echoes.
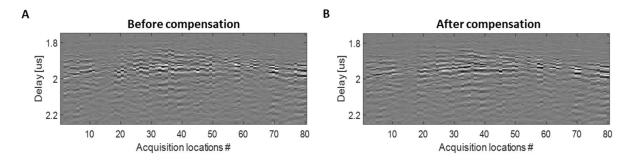
Figure 4-5. (A) Signals at 80 acquisition locations without compensation. (B) Signals at 80 acquisition locations after compensation.

4.3.2 Digital refocusing

Due to the high numerical aperture (NA)-focused transducer applied to the prototype probe, its limited focal zone can become a serious problem, as its depth-of-field is only about 0.5 mm. Inside the small capsule-shaped probe, no mechanical refocusing process can be performed through raster scanning in the axial direction of the transducer. The lateral resolution created by the focused transducer in the B-scan image decays significantly in the out-of-focus region. Several efforts have been made to alleviate the blurring and enlarge the imaging range, including the synthetic aperture focusing technique (SAFT) weighted by a coherent factor (CF) (Liao, Li et al. 2004, Li, Zhang et al. 2006, Deng, Yang et al. 2011, Park, Jeon et al. 2016, Cai, Li et al. 2017) and deconvolution-based methods (Yu, Zhang et al. 2012, Chen, Lin et al. 2013, Kim, An et al. 2013, Cai, Li et al. 2016). Most deconvolution algorithms require the depth-dependent point spread function (PSF) to be known and rely on high SNR. Therefore, 1D SAFT-CF was applied in this study as the digital focusing solution used to enhance lateral resolution. The principle of the SAFT is demonstrated in Figure 4-6.
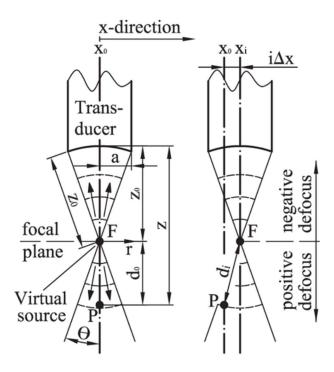
Figure 4-6. Principle of synthetic aperture focusing technique.
(Rupitsch, Maier et al. 2006)

The 2D image $I_{SAFT}(x, z)$ can be reconstructed from the original A-scan PA image $p_{x_i}(t)$

by:

$$I_{SAFT}(x, z) = \sum_{i=1}^{N} p_{x_i}\left(t + \Delta t_i(x)\right)\bigg|_{t=\frac{z}{v_s}} \qquad\qquad 4\text{-}1$$

where N is the number of scanning positions that should be considered. The points located

outside the focusing pattern of scanning step i will not have any contribution to the signal

acquired at step position x_i. The time delay Δt_i can be calculated as:

$$\Delta t_i(x) = sgn(z - z_0)\frac{d_i - |z - z_0|}{v_s}. \qquad\qquad 4\text{-}2$$

where z_0 is the focal depth of the transducer and $d_i = \sqrt{(z - z_0)^2 + (x - x_i)^2}$. To further improve the resolution, a coherent factor was applied as a weighting function to suppress the side-lobes in the image of $I_{SAFT}(x, z)$ by (Hollman, Rigby et al. 1999, Li, Zhang et al. 2006):

$$I_{SAFT-CF}(x, z) = I_{SAFT}(x, z) \cdot CF(x, z)$$ 4-3

where $CF(x, z)$ is defined as:

$$CF(x, z) = \left.\frac{\left|\sum_{i=1}^{N} p_{x_i}(t + \Delta t_i(x))\right|^2}{N \sum_{i=1}^{N} p_{x_i}(t + \Delta t_i(x))^2}\right|_{t=\frac{z}{v_s}}.$$ 4-4

The performance of the SAFT-CF on the developed AR-PAM probe was tested with phantoms and is displayed in Figure 4-7 (A) and (B). As shown in Figure 4-7 (C) and (D), at a depth of 1 mm deeper than the focal depth, the axial and lateral resolutions were determined to be about 65 µm and 90 µm, respectively.
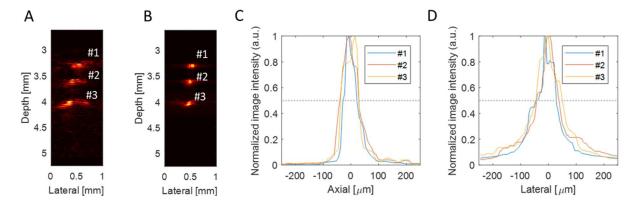
Figure 4-7. (A) and (B) PA images show cross-sections of 50 μm nichrome wires at different depths before and after applying SAFT-CF, respectively. (C) Axial profiles for three targets labeled in (A) and (B) with an averaged FWHM of 65 µm. (D) Lateral profiles with an averaged FWHM of 90 µm.

4.3.3 Obtaining PA molecular component images

Two wavelengths (720 nm and 1310 nm) were selected for characterizing the hemoglobin in inflammation and the collagen in fibrosis. The 1220-nm wavelength was not used in this study because, unlike in human specimens, there is no extra lipid content in rabbit colons, be they diseased or not. Under the homogeneous-perturbation assumption made in Chapter 3, the non-uniform light distribution due to light attenuation and scattering in the homogeneous background at both wavelengths was calculated using Monte Carlo simulation (Figure 4-8 [A] and [B]). The 1D light fluence distribution along the transducer-focusing axis (red dashed lines in A and B) was calculated by averaging the cross-section with a diameter of 1 mm at each depth.
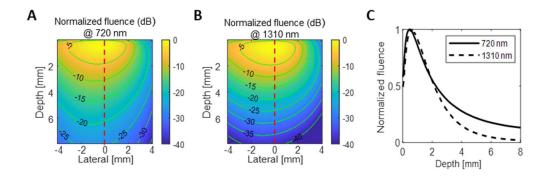
Figure 4-8. (A) Monte Carlo-simulated 2D light fluence distribution in the scanning plane, including the transducer-focusing axis at a wavelength of 720 nm. (B) 2D light fluence distribution at a wavelength of 1310 nm. (C) 1D light fluence distribution along the transducer-focusing axis.

The optical properties applied in the simulation were slightly different from those considered for human bowel tissue. The estimated concentrations of water, lipids, and hemoglobin were 85%, 10%, and 1%, respectively. The optical properties used for light fluence simulation and further calculations are listed in Table 4-1.

Table 4-1. Optical parameters in Monte Carlo simulations

Wavelength	Absorption Coefficient μ_a	Reduced Scattering Coefficient μ_s'	Scattering Anisotropy g
720 nm	$0.04\ cm^{-1}$	$11.8\ cm^{-1}$	0.95
1310 nm	$1.31\ cm^{-1}$	$5.00\ cm^{-1}$	0.95

After the compensations and SAFT-CF reconstruction, the PA molecular component images representing the relative concentration maps of hemoglobin and collagen were generated pixel-wise using:

$$\begin{bmatrix} c_{Hb} \\ c_{cg} \end{bmatrix} = \begin{bmatrix} a_{Hb720} & a_{cg720} \\ a_{Hb1310} & a_{cg1310} \end{bmatrix}^{-1} \times \begin{bmatrix} \mu_{720} \\ \mu_{1310} \end{bmatrix} \qquad 4\text{-}5$$

where μ_i is the total optical absorption at wavelength i (720 nm and 1310 nm), which is proportional to the PA intensity; a_{ji} is the absorption coefficient of certain molecular component j (*Hb*: hemoglobin; *cg*: collagen) at wavelength i; and c_j is the relative concentration of molecular components j.

4.4   Animal Validation with TNBS Rabbit Model *in vivo*

4.4.1 Rabbit model preparation

The animal imaging protocol used in this study was approved by the Institutional Animal Care and Use Committee at the University of Michigan. The endoscopic probe was tested *in vivo* using young (75-to-100-day old) New Zealand white rabbits of both sexes (Covance, Kalamazoo, MI, USA; or University of Michigan, ULAM Breeding Colony, Ann Arbor, MI, USA). The rabbits were placed under general anesthesia using 4-5% inhaled isoflurane during all

procedures. Vital signs and anesthesia depths were continuously monitored. To induce acute inflammation, a single intrarectal dose of 40 mg of TNBS in 25% ethanol was delivered 7 cm into the rectum/distal colon using a 10 French-size feeding tube. To induce intestinal fibrosis, multiple intrarectal doses of TNBS (from 40 to 165 mg) with a 2–4-week healing interval were used to replicate the cycles of inflammation and tissue repair that trigger fibrosis, as have been observed in the rat TNBS model (Kim, Johnson et al. 2008, Stidham, Xu et al. 2011, Dillman, Stidham et al. 2013, Dillman, Swanson et al. 2014, Lei, Johnson et al. 2016, Zhu, Johnson et al. 2018).

4.4.2 Scanning procedure

As shown in Figure 4-9, the rabbits were scanned in a uniform recumbent left-sided position. The probe surface was covered by ultrasound gel and surgical lubricant before being inserted into the rectums of the rabbits. The probe was positioned at the treated segment by repeating the insertion distance of the TNBS delivery (7 cm). The 4-mm longitudinal B-scan using 2-wavelength PA modalities sequentially took a total of eight minutes. Statistical analysis was conducted based on the averaged pixel intensities of the hemoglobin and collagen images. At the

end stage of the imaging sequence, the rabbits in both groups were euthanized by sodium

pentobarbital, administered intravenously.
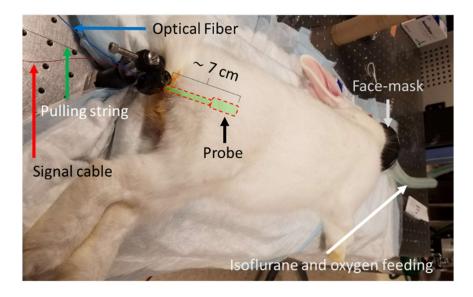
Figure 4-9. Photograph of rabbit and partial experimental setup during *in vivo* scanning.

4.4.3 Comparison between normal, acute, and chronic TNBS models using PA imaging

Eight male and four female young New Zealand rabbits were randomly divided into two

groups. Before receiving any administration of TNBS, a baseline scan was performed with the

prototype capsule probe. The first group of five rabbits received a single 40-mg/kg dose of

TNBS. The *in vivo* colonoscopic imaging was conducted two days after TNBS administration,

when the acute intestinal inflammation condition reached its peak. The second group of seven

rabbits received three cycles of escalating TNBS doses at 40, 80 and 160 mg/kg over two

months. The imaging was conducted 2–5 days after the third TNBS treatment.

4.4.4 Longitudinal study of disease progression in the chronic TNBS model using PA imaging

To test the utility of the PA probe for tracking disease development from acute inflammatory to chronic fibrotic diseases, a longitudinal study was performed with four animals from the chronic cohort. These rabbits received treatments identical to those for the chronic group in Section 4.4.3, but they were performed with four *in vivo* scans during the two months. The timeline for the TNBS treatments and *in vivo* PA scans is illustrated in Figure 4-10. For each rabbit, the first *in vivo* image was acquired prior to the first TNBS treatment (T1) as the baseline. The second image was acquired two or three weeks after T1 but right before T2. The third image was acquired three or four weeks after T2 but right before T3. Rabbits were euthanized after the fourth image, at week 8.
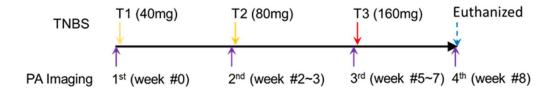
Figure 4-10. Timeline of TNBS treatments and PA scans.

4.4.5 Histology

The distal colons of the euthanized rabbits were harvested and processed for histology. Hematoxylin and eosin (H&E) staining and Masson's trichrome staining were performed by the University of Michigan Cancer Center Histology and Immunoperoxidase Lab (Ann Arbor, MI, USA) and the McClinchey Histology Lab (Stockbridge, MI, USA), respectively. Digital photomicrographs of proximal and distal colon sections were captured using an Olympus BX51 microscope at the University of Michigan Microscopy and Image Analysis Laboratory (Ann

Arbor, MI, USA). The amount of collagen content was quantified from the trichrome-stained slides through a commercial color deconvolution algorithm by a board-certified veterinary pathologist. Three to four random sections of lamina propria were quantified for each slide. A dense fibrosis score was defined as the sum of the percent strong and percent moderate staining per slide.

4.4.6 Results

Colons from acute vs. chronic TNBS-treated animals were roughly similar, with large areas of tissue damage and edema, as illustrated in Figure 4-11 (A). Marked histology differences were observed in the distal colon between the acute and chronic animals. As detailed in Figure 4-11 (B), acute disease was characterized by areas of epithelial loss, ulceration, edema, and extravasation (leakage) of red blood cells from small vessels within the lamina propria and submucosa. While red blood cell extravasation was observed in tissues from chronic animals, areas of epithelial regeneration and collagen scarring were also observed. Fibrosis scores as determined by quantification in trichrome-stained sections and its statistical analysis are shown in Figure 4-11 (C).
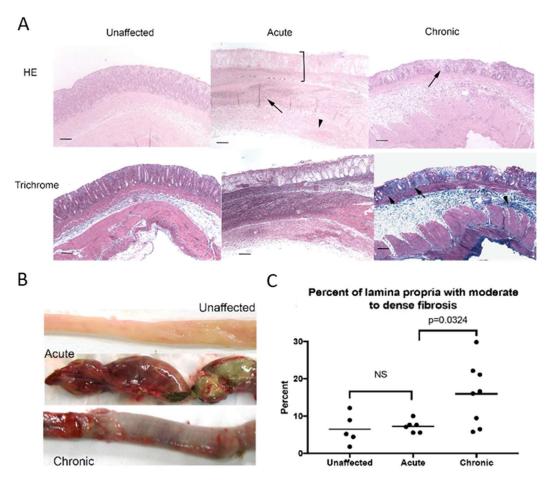
Figure 4-11. (A) Histologic appearance of tissue from normal (untreated), acute, and chronic colon injury. In H&E stained sections of acute injury, there is coagulation necrosis of the mucosa (bracket), inflammatory infiltrate (arrow), and hemorrhage (arrowhead). Chronic injury is characterized by widespread replacement of the mucosa by fibrous connective tissue (arrows) and increased density of fibrosis in the submucosa (arrowhead), not present in normal or acute sections. Bars are 150 microns. (B) Gross appearance of unaffected, acute, and chronic injury. (C) Fibrosis scores as determined by quantification in trichrome-stained sections.

Figure 4-12 (A) shows the representative PA molecular component images for distal colons from normal rabbits, as well as acute and chronic models, respectively. Hemoglobin distributions were plotted in red, while collagen distributions were plotted in green. Figure 4-12 (B) shows the increase of hemoglobin content in both the acute and chronic models compared to the control

54

animals. Figure 4-12 (C) shows the significantly increased fibrosis (relevant to more collagen content) in the chronic model compared to the other two conditions. Both findings in the PA images agree with the pathology. A significant increase of hemoglobin signal intensity ($p = 0.0189$) was found in the acute animals compared to the normal animals. A four-fold collagen signal intensity increase ($p = 0.0002$) was found in the chronic animals compared to the acute animals. These quantitative results agree with the histological quantification.
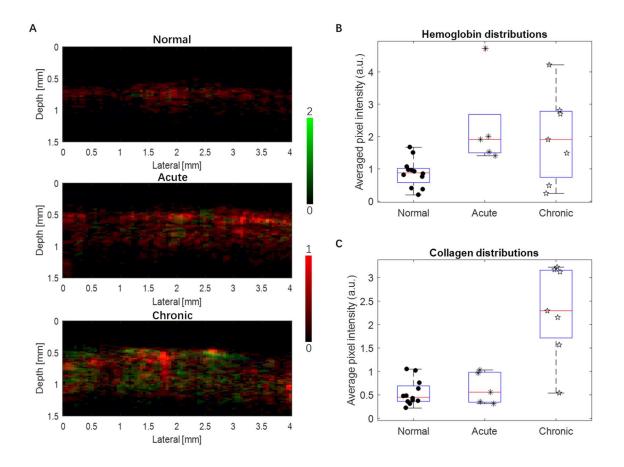
Figure 4-12. (A) Representative PA molecular component images for distal colons of normal, acute, and chronic rabbits. Hemoglobin distributions are plotted in red, and collagen distributions are plotted in green. (B) The boxplots of averaged intensities of hemoglobin distributions for normal, acute, and chronic images. (C) The boxplots of averaged intensities of collagen distributions for normal, acute, and chronic images.

Figure 4-13 (A) displays the obtained PA molecular component images scanned at different stages for one of the four rabbits. Figure 4-13 (B) shows the increasing collagen components over time, which indicates the development of fibrosis due to cycles of inflammation and tissue repair. A correlation of 0.798 was found between the imaged collagen components according to the index of the four PA scans (shown in Figure 4-10) made over the whole course of TNBS treatment.
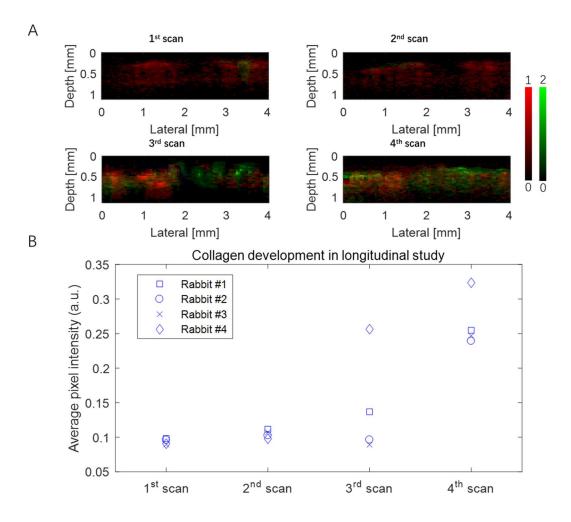
Figure 4-13. (A) Obtained PA molecular component images for rabbit #4 at different scans. (B) Averaged intensities of collagen distributions generated from the four scans applied during the whole longitudinal study. Collagen development was detected in two of the four rabbits in the third scan, and all rabbits had a strong collagen signal one or two weeks after the third treatment.

4.5 Discussion

The TNBS rabbit model used in this study developed similar disease conditions compared to the TNBS rat model used in Crohn's diseases studies. One major difference between the rabbit model and the rat model is the lack of lipid components in healthy and diseased colon tissues of rabbit models. Therefore, the 1220 nm wavelength targeting lipid content was removed, and only 720 nm and 1310 nm were applied to target hemoglobin and collagen in PAI. Quantitative histology analysis demonstrated that the collagen content in chronic subjects increased four-fold compared to the acute subjects.

To resolve the conflict between the demands of high resolution and larger depth-of-field caused by the focused US transducer, the SAFT-CF method, which considers the reception aperture of the US transducer, was implemented to improve resolution in out-of-focus regions. Before the reconstruction, the spatial mismatch between the measurements caused by animal movement in the *in vivo* scenario was corrected under the assumption that a comparable signal phase could be found between neighboring measurements.

Quantitative analysis of the PA measurements revealed the capability to quantitatively differentiate between inflammatory and fibrotic conditions, and to detect collagen deposition during the progression of fibrosis. The obtained PA molecular component images were based on the presence of hemoglobin and collagen, which was consistent with gross pathology and histology. To better improve the imaging performance of the system, a US pulse-echo imaging mode with focused transmission and reception could be integrated in the future for extracting higher-resolution structural information.

Even though the improved depth-of-field was sufficient to cover the thickness of the rabbit bowel wall, it remains difficult to cover the whole thickness of human intestinal strictures (up to

7 mm). To eventually integrate the probe in colonoscopy, a transducer with a larger focal length may be necessary. Under the constraints of capsule dimensions, a trade-off between the transducer's focal length and lateral resolution should be considered.

4.6 Summary and Conclusion

In this chapter, the prototype capsule-shaped AR-PAM probe, developed to enable side-view scanning of the bowel wall, was discussed. Motion artifacts due to intestinal peristalsis were compensated for to improve image quality. The problem of limited depth of field caused by the highly focusing transducer was resolved by a digital focusing method that provided a lateral resolution of 90 μm over an improved depth-of-field of 1.5 mm. The capability of the probe to quantitatively differentiate the pathological conditions of CD was validated in the rabbit model *in vivo*. The longitudinal measurements on rabbits investigated the feasibility of monitoring the development of fibrosis in early and refractory conditions, which could in turn provide valuable information for decision making during CD management.

Chapter 5

Monitoring Dose Delivery during External Beam Radiation Therapy by X-ray Acoustic Imaging Technique

In the following chapters, an x-ray-based thermoacoustic imaging is proposed for monitoring dose delivery during radiation therapy. The terms *photon* and *beam* are used to describe the x-ray photons and beams generated by the radiation source, respectively.

5.1 Introduction

As one of the main treatment options for cancer, radiation therapy is given to roughly two-thirds of all cancer patients (Oncology 2008). The therapy works by damaging the DNA of cancer cells using high-energy beams of ionizing radiation (Podgorsak 2003, Podgoršak 2006). Primarily, clinical linear accelerators (Linac), which produce high-energy megavoltage photons or electron beams, are used to deliver ionizing radiation to patients from outside the body during external beam radiotherapy (EBRT). However, radiation damages not only cancerous tissues but healthy cells as well. Therefore, the premise of radiation therapy is to optimize a strategy for maximizing damage to cancer cells while minimizing damage to the surrounding healthy regions.

The demand for delivering the correct dose to the proper location inside a patient's body has led to more advanced treatment delivery techniques, such as intensity modulated radiation

therapy (IMRT) and volumetric-modulated arc therapy (VMAT) (Webb 2001, Lehnert 2008, Hall and Giaccia 2012). However, the complication due to organ deformations and respiratory motion still cannot be avoided (Intensity Modulated Radiation Therapy Collaborative Working Group 2001, Sterzing, Engenhart-Cabillic et al. 2011, Timmerman and Xing 2012). Therefore, employing a volumetric form of *in vivo* dose measurement is necessary to assess clinically relevant differences in the delivered intensity and delivery location between the planned and delivered radiation dose.

Several techniques for real-time *in vivo* dosimetry are currently used to monitor the radiation dose delivery during EBRT (Mijnheer, Beddar et al. 2013, Mijnheer, Olaciregui-Ruiz et al. 2013), including silicon diodes (Huyskens 2001), metal oxide semiconductor field effect transistors (MOSFETs) (Chuang, Verhey et al. 2002, Ramaseshan, Kohli et al. 2004), and electronic portal imaging devices (EPIDs) (van Elmpt, McDermott et al. 2008, Mans, Remeijer et al. 2010). However, the silicon diodes and MOSFETs are point dosimeters, and the EPIDs are not accurate enough due to their exit dose nature and lack of sufficient sensitivity (Jornet, Carrasco et al. 2004, Mijnheer, Beddar et al. 2013).

According to the principle of thermoacoustic (TA) techniques, pulsed x-ray beam generated from Linac should be able to induce x-ray acoustic (XA) waves through the TA effect. As stated in Section 2.3, a measured XA signal can be applied to resolve the heat absorption distribution caused by the radiation, which only describes the distribution of the dose except for a factor of local density. As ultrasound detection is easy to implement and does not perturb the radiation treatment, XA imaging may represent a potential method for relative and *in vivo* dosimetry.

Recently, the detection of XA signals in a clinical Linac has been demonstrated, and the XA computed tomography (XACT) imaging of a lead rod embedded in chicken breast tissue has

60

been achieved (Xiang, Han et al. 2013). Lately, the ability to form experimental XACT images in pure water in a variety of clinically relevant situations and to extract accurate dosimetric information from such images was also demonstrated (Hickling, Lei et al. 2017). Besides studies that have worked with high-dose x-rays generated by Linac, XACT imaging based on kV x-ray excitations has also been explored (Tang, Nguyen et al. 2017, Shanshan, Kai et al. 2018). These results inspired the author to further develop and assess the performance of the XA imaging technique using more realistic soft-tissue phantoms.

In this chapter, the feasibility of monitoring dose delivery via the XA imaging technique during external beam radiation therapy was investigated. A prototype XACT system was established and tested with phantoms made from biological tissues. A physical correlation between the relative dose and XA image intensity was derived, and the practical challenges to achieve more accurate dose monitoring were addressed. The sensitivity of XACT in monitoring and quantifying the delivered dose was also explored. The potential of XACT to track the position of the radiation dose and measure beam–target misalignments was demonstrated.

5.2 Experimental Setup

Unlike the nanosecond laser pulse applied in PA imaging, clinical Linacs offer an excitation source with a relatively long pulse duration of $3-6\,\mu s$ (Kainz 2006, Hickling, Léger et al. 2016). In order to satisfy the stress confinement given by eq. (2-11), the expected spatial resolution of XA imaging is about several millimeters(Xia, Yao et al. 2014, Zhou, Yao et al. 2016). Therefore, a transducer with a 0.5-MHz central frequency was selected as the detector to cover the more low-frequency range where the XA signal would be located. A single-element

circular-scanning computed tomography system was applied to achieve the XA imaging with the selected transducer.

Figure 5-1 shows the schematic diagram and a photograph of the prototype XACT system developed at the author's institution. A clinical radiotherapy Linac (TrueBeam™, Varian Medical Systems) provided 6-MV photon beam pulses with a 4-μs pulse duration and operated at a dose rate of 800 MU/min. An unfocused immersion transducer (V301, Olympus-NDT) with a central frequency of 0.5 MHz and a –6 dB bandwidth of 64% was driven by a computer-controlled stepper motor (MD2, Arrick Robotics) to scan around the phantom inside a water tank. The transducer was used to detect the XA waves generated from the phantom and transmitted through water at each scanning position. The output of the transducer was amplified by the preamplifier (5660B, Olympus-NDT), which was set to a gain of 60 dB with a bandwidth from 50 kHz to 2 MHz, and then recorded by a 14-bit digitizer card (Razor 14, GaGe) inside a PC located outside the treatment room. The acquisitions were triggered by the Linac's target pulses, which were sent out from the Linac console, and were operating at a 10-MHz sampling frequency. To scan a 2D image, the transducer rotated along an entire circle (diameter 12 cm) around the phantom with a total of 120 equiangular steps. The measurement at each scanning position was averaged over 660 pulses, and the signal acquisition for a 2D image took about 10 minutes. To avoid the attenuation of the radiation beam passing through the rotation stage, the gantry was rotated 180° so that the beam came from the bottom of the water tank.
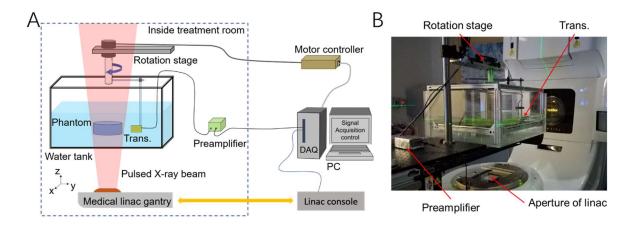
Figure 5-1. (A) Schematic of the XACT system. (B) Photograph of the instruments inside the treatment room. Trans.: transducer; DAQ: data acquisition card.

5.3 Information from XACT Imaging

5.3.1 Relative dose distribution

The signals recorded at each scanning position were processed with a median filter before calculating the average to reduce electrical noise. A digital high-pass filter with a cut-off frequency at 50 kHz was applied to remove DC and low-frequency background drift inside the averaged signals, and a Savitzky-Golay denoising filter (order of 3, window of 31) was applied to further smooth the signals before reconstruction. In the case of the 2D XACT applied in this study, the images on the scanning plane were reconstructed based on a simple filtered back-projection algorithm following eq. (2-20). Therefore, the reconstructed XA intensity $I(\boldsymbol{r})$ can be written as:

$$I(\boldsymbol{r}) = p_0{}^b(\boldsymbol{r}) \propto \Gamma(\boldsymbol{r})H_d(\boldsymbol{r}).$$

5-1

The heat absorption distribution $H_d(\boldsymbol{r})$ can be expressed with the delivered dose:

$$H_d(\boldsymbol{r}) = \frac{\eta_{th}(\boldsymbol{r})\rho(\boldsymbol{r})}{\tau_p} D_p(\boldsymbol{r}) \qquad\qquad 5\text{-}2$$

where $D_p(\boldsymbol{r}) = D_r(\boldsymbol{r}, t)\tau_p$ is the dose distribution due to a single x-ray pulse, under the short

pulse assumption. Then, the dose distribution D_p can be related to the XACT image intensity

by:

$$D_p(\boldsymbol{r}) \propto D_p'(\boldsymbol{r}) = \frac{I(\boldsymbol{r})\tau_p}{\Gamma(\boldsymbol{r})\eta_{th}(\boldsymbol{r})\rho(\boldsymbol{r})} \qquad\qquad 5\text{-}3$$

From this equation, the relative dose distribution $D_p{}'$ can be calculated directly, if the

local Grüneisen parameter, density, and thermal efficiency are known. Since the initial

pressure is calculated relatively in eq. (5-1), a secondary standard is required to calibrate the

XA image intensity to the absolute dose.

5.3.2 Absorption coefficient

The absorption coefficient is already considered in the dose-producing process, but its

influence in dose delivery or contrast of XA imaging is not significant. The x-ray photons,

especially the MVs photons utilized in EBRT, do not show strongly different absorptions in

different soft tissues. Hence, the XACT image does not yield enough information about the

spatial absorption coefficient $\mu_a(\boldsymbol{r})$ in tissue. The absorption coefficients of x-rays with 1

MeV of photon energy in some materials are listed in Table 5-1 (Hubbell and Seltzer 1995).

Table 5-1. Density and x-ray (1 MeV) absorption coefficients of various materials

Material	Blood	Bone	Brain	Lung	Muscle	Water	Lead
Density $\rho\ [g/cm^{-3}]$	1.06	1.92	1.04	1.05	1.05	1.00	11.4
Absorption coefficient $\mu_a\ [m^{-1}]$	7.43	12.6	7.32	7.36	7.36	7.07	80.6

One of the main challenges to the further application of XA imaging is that XA signals are very weak. In blood, the absorption coefficient of a 1-MeV photon is one order smaller than a 720-nm photon. Previous works acquired their XACT images by taking advantage of the high absorption in lead (Xiang, Han et al. 2013, Kim, Park et al. 2017) or gold (Xiang, Tang et al. 2016), but increasing the absorption coefficient in clinics is far more difficult.

5.3.3 Grüneisen parameter

The small difference in x-ray absorption makes the variations in Grüneisen parameters notable in XACT. Given that the Grüneisen parameters of fat are about seven times larger than those of blood at room temperature (Yao, Zhang et al. 2014), fatty tissue will have a positive contrast in XA images. Meanwhile, the spatially varying Grüneisen parameters will represent the main obstacle in determining the relative dose. A simple phantom study was conducted to show the influence of the Grüneisen parameter difference. As shown in Figure 5-2, a block of porcine gel (10g/100ml, G2500, Sigma-Aldrich) contains one fat cuboid ($3 \times 3 \times 2\ cm^3$) and one muscle cuboid ($3 \times 3 \times 2\ cm^3$). Figure 5-2 (B) shows the XACT image acquired when a 6 MV x-ray beam with a size of $12\ cm \times 12\ cm$ shooting from top as the red dashed square shown in Figure 5-2 (A), Figure 5-2 (C - E) show the XACT images acquired with the

$3\,cm \times 3\,cm$ squared beam fields covering the gray, green, and blue dashed squares, respectively.

When a large beam was applied, only the shape of the fat cuboid can be observed inside the field of the beam. This is because of the high Grüneisen parameter of the fat compared with the muscle and the gel. When a small beam was applied on different materials (i.e., gel, fat, and muscle), the intensities presented by the XACT images are strongly different. This result demonstrates that, even when the dose deposition is the same, the induced XA signal may be largely different because of the differences in Grüneisen parameters in target tissues. The differences in Grüneisen parameters can be utilized to present the endogenous tissue contrast in XA images, while the spatially varying Grüneisen parameters can also be a challenge in determining the delivered dose during radiation therapy by performing XACT.
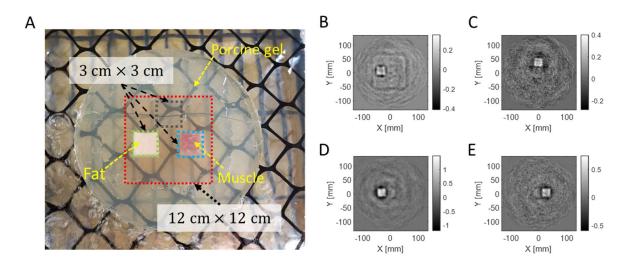
Figure 5-2. (A) Fat cuboid and muscle cuboid embedded inside a block of porcine gel. (B) XACT image acquired under x-ray beam with a size of $12\,cm \times 12\,cm$ shown as red dashed square in (A). (C - E) XACT images acquired under x-ray beam with a size of $3\,cm \times 3\,cm$ locating at gray, green, and blue dashed squares, respectively.

5.3.4 Beam boundary

The x-ray beams used in radiation therapy usually have sharp spatial boundaries and a flat-top spatial profile. For x-ray induced signals, eq. (3-6) can be written as:

$$p(t) = \frac{1}{4\pi v_s^2}\frac{\partial}{\partial t}\int dr \frac{1}{r}\frac{\Gamma(\boldsymbol{r})\eta_{th}(\boldsymbol{r})\rho(\boldsymbol{r})}{\tau_p} D_p(\boldsymbol{r})\delta\left(t - \frac{r}{v_s}\right) \qquad 5\text{-}4$$

Since the absorption rate has no large variation, and the absorbers are almost uniformly distributed inside the beam, the XA image is usually speckle-free (Guo, Li et al. 2009). According to eq. (5-4), when the low-frequency components corresponding to the volume information are not acquired, the detected XA signals are only from the discontinuities, such as the interface between dissimilar materials or beam boundaries. This loss of low-frequency may cause a strong edge-enhancing effect when imaging large objects or using large beams. Figure 5-3 (A) shows the XACT image for a $4\ cm \times 4\ cm$ 6 MV x-ray beam field in water. In Figure 5-3 (B), the intensity profile acquired along the dashed line in Figure 5-3 (A) shows the 25% to 75% distance of the edge response as 5.8 mm, which presents the spatial resolution of the system. The top of the intensity profile is curved in, as the system cut-off the low-frequency components lower than 50 kHz. In the ideal situation when the detection system can cover both low-frequency and high-frequency spectra, the reconstructed image in Figure 5-3 should have a flat top as well as the sharp edges. Although the beam boundary information is sufficient for revealing the spatial information of the beam and the object, inaccurate measurement of the XA intensities in the center of the beam or the object can be a problem in estimating the dose distribution $D_p(\boldsymbol{r})$.
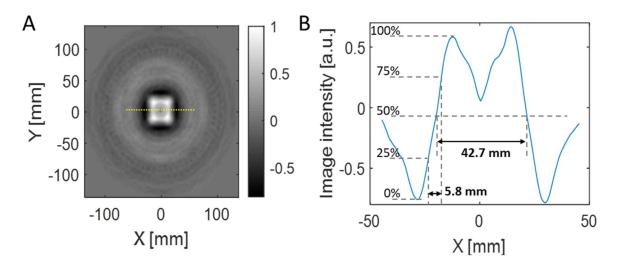
Figure 5-3. (A) XACT image of a $4\ cm \times 4\ cm$ beam field in water. (B) Intensity profile along the yellow dashed line in (A), including the edge spread function.

5.4 Experiments and Results

5.4.1 Dose delivery estimation

The dose deposition in the target tissue is dependent on the penetration of the x-ray beam through the tissues above the target. As shown in Figure 5-4, the intensity of the x-ray is presented in red with a gradient to indicate increasing depth into the tissue. Target 2 is located deeper compared to Target 1, so the dose delivered to Target 2 should be smaller than that delivered to Target 1. Target 3 is located at the same depth as Target 1, yet the dose delivered to Target 3 is much smaller than that delivered to Target 1 due to the strong scattering and attenuation caused by the bone located above Target 3. The first step of this procedure was to validate the feasibility of assessing the difference in dose delivery at target regions using XACT.

68
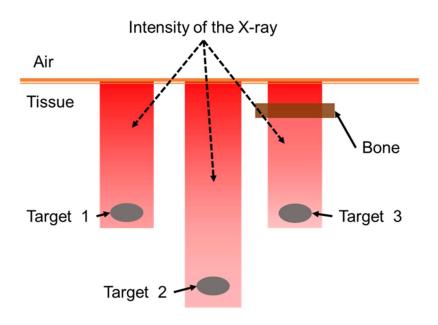
Figure 5-4. Schematic of dose delivery to targets in different situations.

5.4.1.1 Experiment with wedged radiation beams

To evaluate the sensitivity and accuracy of the XACT system in measuring different doses

delivered to different targets, a phantom with a row of five cylinders (diameter: 1 cm; height: 2

cm) made with lard and fixed inside porcine gel (10g/100ml, G2500, Sigma-Aldrich) was

prepared, as shown in Figure 5-5. Three physical wedges (constructed from steel) with different

attenuation slopes (15°, 30°, and 45°) were added to the Linac aperture, and the differences in

dose delivery to the five lard cylinders were measured by the XACT system. The center plane of

the lard cylinders and the scanning plane of the transducer were adjusted to the same height with

a 100-cm SSD 10 cm above the bottom of the tank. Since the five lard cylinders were prepared

with the same material, the difference in the absorbed dose due to the material properties can be

ignored. Therefore, the intensities in the XACT image can directly reflect the local doses at the

five lard cylinders. For statistical analysis, 10 independent measurements were conducted for

each of the three wedges. The dose distributions at the imaging plane were also recorded by radiochromic film for comparison and validation.
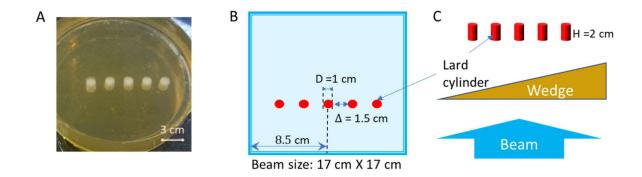
Figure 5-5. (A) Photograph of a porcine gel phantom containing five identical lard cylinders distributed along a row. (B) Schematic diagram of the lard cylinders and radiation beam (top view). (C) Schematic diagram of lard cylinders, wedge, and radiation beam (side view). D is the diameter of the lard cylinder; Δ is the space between two adjacent cylinders; H is the height of the lard cylinder.

Figure 5-6 shows XACT imaging results from the phantom containing five lard cylinders under 6-MV photon beams. The only difference between Figure 5-6 (A) and (B) is that a 30° physical wedge was added to the Linac aperture for the image in Figure 5-6 (A), while no wedge was used for the image in Figure 5-6 (B). The image intensity was normalized to the maximum intensity of the image, which was acquired without using the wedge. To explore the feasibility of XACT in quantifying the deposited dose in each cylinder target, the intensity profiles extracted from the two XACT images were compared in Figure 5-6 (C). Considering that the five cylinder targets were not perfectly aligned along a horizontal line, each intensity profile actually shows the horizontal projection of the maximum value inside the range from $y = -40mm$ to $y = -20mm$.
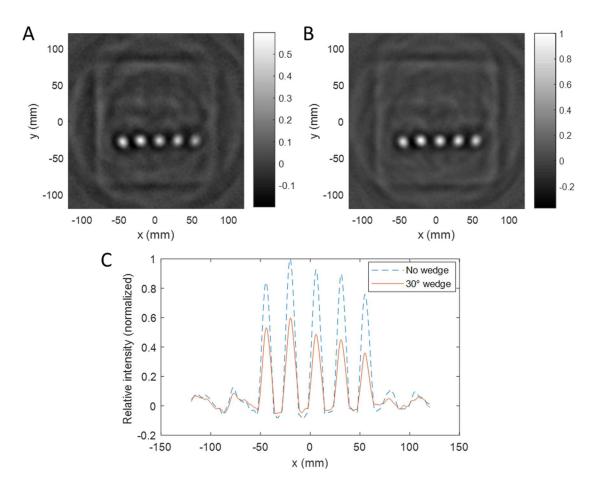
Figure 5-6. (A) A reconstructed XACT image of the phantom containing five
lard cylinders. A 30° physical wedge was used to change the dose applied to
each cylinder target. (B) A reconstructed XACT image of the same phantom
where no wedge was applied. (C) The intensity profiles along the x-axis
showing the deposited doses in the five cylinder targets for the two situations,
i.e., with and without using the 30° wedge.

Figure 5-7 (A - C) present the quantified datasets of relative XA intensities for the five

lard cylinders imaged with the use of a 15° physical wedge, a 30° physical wedge, and a 45°

physical wedge, respectively. Under each condition (i.e., three different wedges for the results

in A-C, respectively), the normalized relative intensity of each of the five lard cylinders was

quantified by dividing its maximum intensity in the XACT image by the maximum intensity

of the corresponding lard cylinder from the XACT image that did not use a wedge. Under each

condition, 10 independent measurements were conducted for statistical analyses.
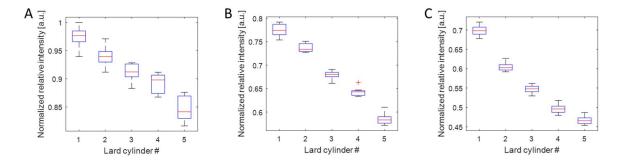
Figure 5-7. Normalized relative XA intensities for the five lard cylinders when
(A) a 15° physical wedge, (B) a 30° physical wedge, or (C) a 45° physical
wedge was used. Ten independent measurements were conducted to compute
the mean and the standard deviation for each lard cylinder under each
condition.

Figure 5-8 (A) shows the dose profiles per pulse extracted from the film test results in the

same direction as the five lard cylinders were aligned. The dose per pulse was calculated by the

recorded accumulated dose, dividing the monitored pulse number during each film test. For each

wedge, the normalized relative XA intensities of the five lard cylinders shown in Figure 5-7 were

compared with the dose per pulse values read from film profiles at positions of

$-50\ mm, -25\ mm,\ 0, 25\ mm, and\ 50\ mm$, as displayed in Figure 5-8 (A). As derived in

Section 2.2, the XA intensities $I(r)$ for each lard cylinder can be fitted to the local dose $D_p(r)$

measured by the film with a determined constant ξ, which should include the local Grüneisen

parameter, thermal efficiency, mass density, and proportionality considered in eq. (5-3):

$$D_p(r) = \xi \cdot I(r)$$ 5-5

The XA intensities and the dose per pulse are plotted together in Figure 5-8 (B - D), while Figure 5-8 (E) presents the proportionality between the normalized relative XA intensities and the dose per pulse by determining a constant ξ for each wedge. The minimum dose difference between two lard cylinders under the 15° physical wedge is 2.9%, according to the film result shown in Figure 5-8 (B). Based on the dataset shown in Figure 5-7 (A), a *t*-test with a null hypothesis that XACT cannot detect the dose difference between the adjacent lard cylinders achieved a significant *p*-value of 0.02. Therefore, the XACT image can accurately determine the minimum difference in dose delivery between adjacent lard cylinders, which indicated that the sensitivity of XACT imaging in monitoring the relative dose can be achieved up to 2.9%.
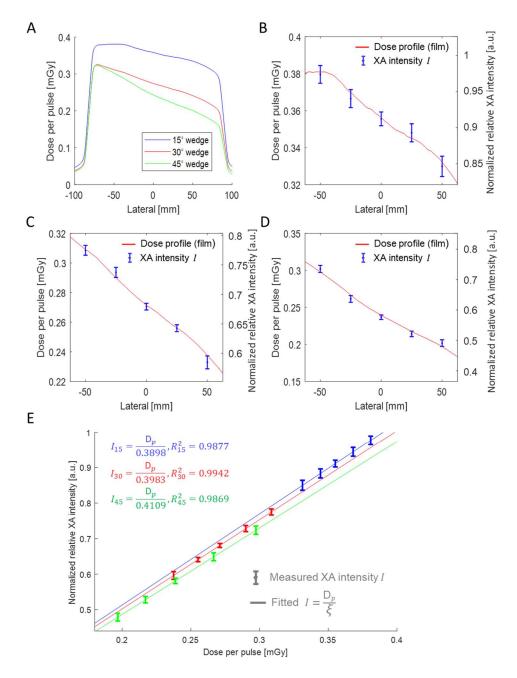
Figure 5-8. (A) Dose profiles extracted from the film test results for three physical wedges (15°, 30°, and 45°). (B)-(D) Dose per pulse extracted from film profiles shown in (A) matched with the mean value and standard deviation of the normalized relative XA intensities (shown in Figure 5-7) under the 15°, 30°, and 45° physical wedges, respectively. (E) Correlation between the normalized relative XA intensity and the film measured dose per pulse for the 15°, 30°, and 45° physical wedges (shown in blue, red, and green, respectively).

5.4.1.2 Experiment with blocked radiation beams

Considering the complex situation inside a patient's body during radiation therapy, the radiation dose reaching the target volume may experience different attenuations, especially when the beam passes through covering tissues containing cavities (less attenuation) and bones (more attenuation). This is another cause for uncertainty in estimating the dose delivered to the target. To simulate this situation and validate the feasibility of XACT in measuring the local dose delivered, a phantom shown in Figure 5-9 was prepared and imaged. Four lard cylinders (diameter: 1 cm; height: 2 cm) were individually covered by a piece of bone (thickness: 0.9 cm), an air gap (thickness: 1.5 cm), a piece of pork muscle (thickness: 1.9 cm), and nothing, and then all were fixed inside porcine gel. Five independent measurements on this phantom were conducted for statistical analysis.
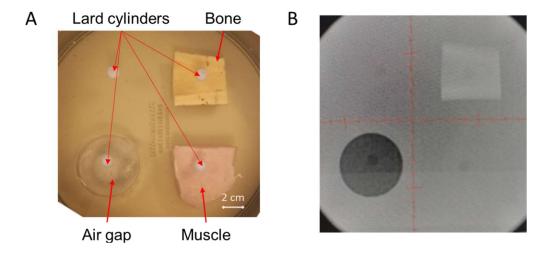
Figure 5-9. (A) Photograph of a porcine gel phantom containing four identical lard cylinders covered by different materials with different x-ray attenuation, including bone, air gap, pork muscle, and nothing (gel only). (B) Radiograph of the phantom.

Figure 5-10 displays one representative reconstructed image and the quantified relative XA intensities of the four lard cylinders inside the phantom shown in Figure 5-9 (A). All

measurements were normalized to the mean value of XA intensities of the lard cylinder without

being covered by anything except for gel. In the case where the x-ray passed through the air gap

before reaching the lard cylinder, the XA intensity from the lard cylinder was about 10%

stronger, as the x-ray experienced lower attenuation inside the air gap compared to gel or water.

The XA intensity from the lard cylinder covered by bone was about 20% weaker, as the x-ray

experienced more attenuation while propagating through the bone (Hubbell and Seltzer 1995).

The p-values calculated from the t-tests comparing any two groups are shown in the figure. All

p-values were smaller than 0.005 except for the p-value from the comparison between the muscle

group and the gel group, which was due to the fact that muscle and gel have similar x-ray

attenuation. The different attenuations of x-ray passing through bone, muscle/gel, and air can be

determined by XACT imaging significantly, which agrees well with the radiography results

shown in Figure 5-9 (B).
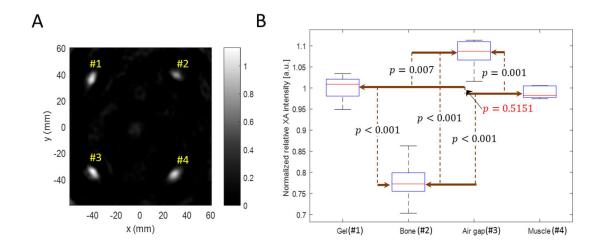
Figure 5-10. (A) A reconstructed XACT image of the phantom shown in Figure 5-9 (A). (B) Statistical analyses of the normalized relative XA intensities for the four lard cylinders covered by materials with different x-ray attenuations, including nothing (gel only), bone, air gap, and muscle. The p-values from the t-tests comparing any of the two groups were evaluated.

5.4.2 Imaging of deposited dose

To validate the feasibility of XACT in verifying the shape and location of the x-ray field during treatment, a phantom containing two pieces of veal liver and one cuboid of fat was prepared, as shown in Figure 5-11. A cuboid of tissue was removed from the larger piece of veal liver and replaced with the cuboid of fat ($6\ cm \times 4\ cm \times 3\ cm$) as the target of treatment. All the tissues were fixed in a block of porcine gel.

Before XACT imaging, an ultrasound (US) image of the phantom was acquired by compounding 12 US B-mode images acquired around the phantom. The 12 B-mode images were scanned by a commercial system (Z.one, Zonare Medical Systems) and a phased array probe (P4-1, Zonare Medical Systems). To acquire images at different locations around the phantom, the probe was driven by the same rotation stage in the XACT system. With a 30° step size, 12 images were scanned along an entire circle around the phantom. In the experiment, the x-ray beam had a field size of $6\ cm \times 4\ cm$, the same as the size of the fat cuboid in the imaging plane. Both the center layer of the phantom and the scanning plane of the transducer were adjusted to satisfy a source-to-surface distance (SSD) of 100 cm. For the first XACT image, the x-ray beam was aligned with the position of the fat cuboid, as shown by Field #1 in Figure 5-11 (B). To mimic the situation whereby an x-ray beam is off-target due to body motions or misplacement errors, the x-ray beam was shifted away from the target during the second round of XACT imaging, as shown by Field #2 in Figure 5-11 (B).
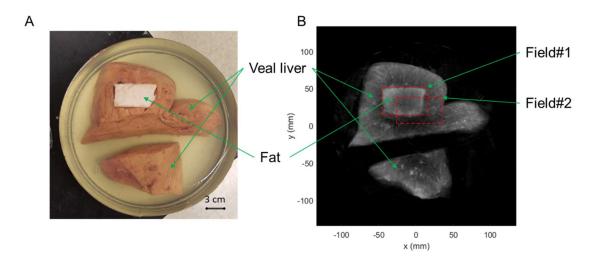
Figure 5-11. (A) Photograph of a porcine gel phantom containing veal liver and fat. (B) Compounding US image of the phantom, where the shape and location of the radiation x-ray beam are labeled by a red dash rectangle ($6\ cm \times 4\ cm$). Field #1: The beam was aligned to the fat cuboid (i.e., target of treatment); Field #2: The beam was shifted away from the target ($20\ mm$ along the x-axis and $-10\ mm$ along the y-axis).

The reconstructed XACT images (normalized so that the maximum intensity equaled 1) corresponding to Field #1 (radiation beam on-target) and Field #2 (radiation beam off-target) are shown in Figure 5-12 (A) and (B), respectively. In Figure 5-12 (A), the entire outline of the fat cuboid can be observed, as the whole fat cuboid was just covered by the x-ray field, and the outlines of both were overlapping. In Figure 5-12 (B), the boundaries of the squared x-ray field can be observed, as the outline of the field shifted from the outline of the fat cuboid. Moreover, one corner of the fat cuboid can also be seen due to the contrast between the fat and the liver tissues. This contrast is mainly caused by the differences in the Grüneisen coefficient, which are 0.6 for fat and 0.15 for liver. Figure 5-12 (C) and (D) show the XA images (pseudo color) superimposed on the compounding US image (gray-scale). These combined images present the positions of the deposited dose (as mapped by XACT images) related to the location and shape of the treatment target (as shown by the US images).
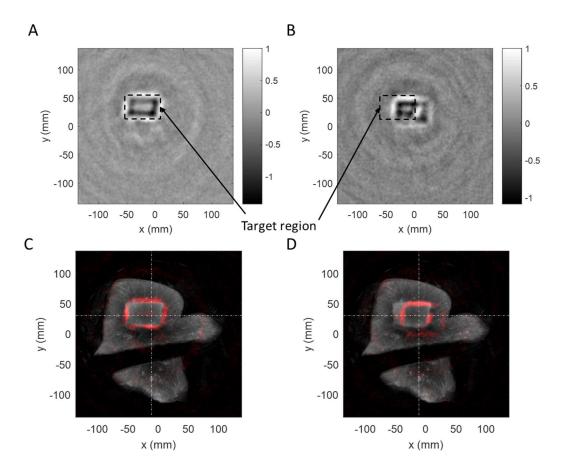
Figure 5-12. Normalized XACT images corresponding to (A) Field #1 (radiation beam on-target) and (B) Field #2 (radiation beam off-target) as described in Figure 5-11 (B). The dashed rectangle marks the position and shape of the target. (C) XACT image in (A) presented in pseudo color and superimposed on the gray-scale US image of the phantom. (D) XACT image in (B) presented in pseudo color and superimposed on the gray-scale US image of the phantom.

Figure 5-13 (A) and (B) display the XACT and US intensity profiles along the dash-dot lines marked in Figure 5-12 (C) and (D). The vertical line is through $x = -14\ mm$. The horizontal line is through $y = 35$ mm. The US intensity profiles present the boundaries of the target. According to the US profiles, the horizontal size and vertical size of the target along the marked lines become 59 mm and 41 mm, respectively, due to the distortion. The two sets of XACT intensity profiles correspond to Field #1 (radiation beam on-target) and Field #2 (radiation beam

off- target), respectively. Compared with the US profiles, the determined boundaries in XACT

profiles labeled with green and red dashed lines display the conditions of beam alignment before

(on-target) and after (off-target) shifting the beam location, respectively. Subject to changes in

the beam location, the horizontal position and vertical position of the beam, as presented by the

XACT intensity profiles, were shifted by $+18\ mm$ and $-9\ mm$, respectively. As shown in

Figure 5-12 and Figure 5-13, the XA intensity peaks at the interfaces, i.e., the boundary of the x-

ray field or the interface between the fat cuboid and the liver. According to eq. (5-4) and

considering the differences between the Grüneisen parameters of fat and liver, the peak of XA

signals corresponding to the field boundary located on fat is higher than the peak from the field

boundary located on liver and the peak at the fat and liver interface.
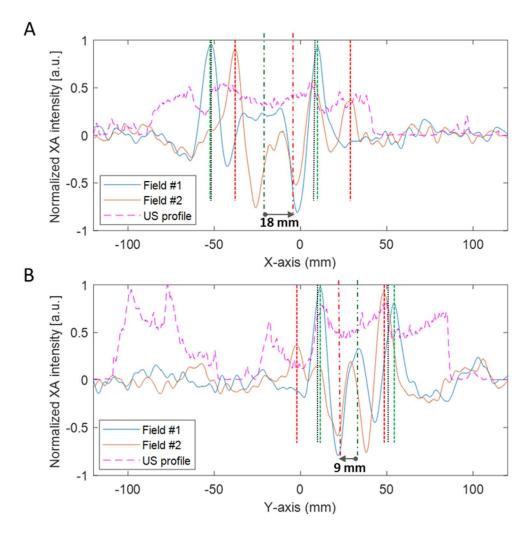
Figure 5-13. The intensity profiles along the marked horizontal line ($y = +35\ mm$) and the vertical line ($x = -14\ mm$) in the XACT images of the two measurements (beam on-target and beam off-target, respectively) and the compounding US image. The green and red dashed lines label the beam boundaries determined by the profiles of XACT images before (on-target) and after (off-target) shifting the beam location, respectively. The green and red dash-dot lines show the centers of the beam (i.e., the central lines between the determined boundaries) before and after shifting the beam location, respectively. The gray dashed lines show the boundaries of the target extracted from the intensity profiles of the US image.

5.5 Discussion

In the experiment, imaging of several phantoms made from biological tissues was conducted using a prototype XACT system utilizing a single flat transducer. Because tomographic imaging was achieved via the rotational scan of the transducer around the phantom, only 2D images in the scanning plane, which was perpendicular to the direction of the x-ray beam, were reconstructed. Therefore, in the preparation of the phantoms, all important features were distributed in a single layer. In the future, however, by scanning around the sample along a 2D surface by, for example, performing a scan along a spherical surface or a cylindrical surface surrounding the sample, a real 3D image can be reconstructed to evaluate the deposited radiation dose in any voxel.

In XACT images, for example, in Figure 5-12, strong XA intensities appeared at the beam field boundaries or at the interface between the tissues. As mentioned in Section 5.3.4, this was mainly due to the limited bandwidth of the measuring system, which missed the low-frequency components. To cover the very low-frequency range, a low-frequency transducer should be selected with a penalty of lower spatial resolution. Besides, the temporal profile of x-ray pulse should also be taken into consideration, since the current duration of the x-ray beam pulse is too long to be treated as a delta function. When possible, decreasing the duration of the x-ray pulse and maintaining the dose amount per pulse from the Linac could enhance both the spatial resolution and the signal-to-noise ratio (SNR).

As demonstrated in Section 5.4.1, the intensity inside the XACT image is related to the energy deposited by the excitation pulse, which implies the possibility of tracking the delivered target dose per pulse independent of the repetition rate of the Linac (~330 Hz at the dose rate of 800 MU/min for a 6-MV beam). However, to achieve a sufficient SNR, the signals detected for XACT imaging had to be averaged 660 times before being used for image reconstruction. When

XA signals need to be collected from 120 scanning positions around the sample, the signal acquisition for each 2D XACT image will take about 10 minutes, and parts of the radiation pulses will be missing due to the movement of the transducer between each scanning position. When a circular array probe or a commercially available linear probe driven by a multi-channel data acquisition system can be used to replace the circular scan of a single element transducer, a 2D XACT image can be acquired over a much shorter time period. Similar to the works shown in Figure 5-8, the intensity of the formed XACT image can be calibrated to the averaged dose deposited by the excitation pulses during the short time interval following eq. (5-5). This would make it possible to track the mGy level variation of the dose delivery with high spatial and temporal resolutions, which would be useful for monitoring complex dose delivery techniques, such as dynamic IMRT, and for realizing the potentials of (4D) time-resolved intrafraction dose delivery (Mijnheer, Olaciregui-Ruiz et al. 2013). The radiation dose at each spatial point will be quantified by the integration of the local XACT intensity over the time intervals. Moreover, as the difference in dose delivery can be determined by XA intensity in real-time or quasi-real-time, any changes affecting treatment efficacy in the target tissue could be monitored during the treatment and be utilized to modify the treatment plan online.

To evaluate the accuracy of monitoring the dose delivered to the target region, different physical wedges were applied to generate different dose distributions on the target region. The relative dose distributions quantified by XACT were correlated with the dose profiles measured by radiochromic films. All the lard cylinders were modeled to the same geometry and fixed along a line inside the porcine gel, which could be treated as a homogeneous background. In this way, a simple back-projection algorithm, one which does not consider any attenuations or distortions during acoustic wave propagations, could be applied to extract the initial pressure.

The uniform Grüneisen parameter, thermal efficiency, and density simplified the relation between the delivered dose and the XA intensity described in eq. (5-3). However, for clinical implementation, all these parameters need to be considered before truly quantitative evaluation of dose can become possible. In future clinical applications, accessing the tissue properties in the volume of interest could be realized via computed tomography (CT) imaging during the treatment planning (Johns and Yaffe 1987). In this way, quantitative or semi-quantitative evaluation and mapping of dose delivery can be achieved.

5.6 Conclusion

In this chapter, the feasibility of applying an XA imaging technique in monitoring dose delivery by clinical Linac was investigated. A prototype XACT system was established to achieve XA imaging on soft phantoms made of biological tissue. A physical correlation between the relative dose and XA image intensity was derived. The potential perturbs and practical challenges in imaging dose distribution with the XA imaging technique were discussed. The XACT images of soft-tissue phantoms can be achieved with accuracy in dose measurements of up to 2.9% and able to track the position of the beam with a spatial resolution of 5.8 mm. This demonstrates the potential application of XA imaging as a novel *in vivo* dosimetric solution for verifying beam alignment in relation to target tissue, and for evaluating the accuracy of doses delivered during EBRT.

Chapter 6

Real-time Monitoring of Radiation Therapy with X-ray Acoustic and Ultrasound Dual-modality Imaging

6.1 Introduction

Following the strategy of delivering maximum radiation doses to the targeted area while minimizing the dose to surrounding healthy tissue (Liauw, Connell et al. 2013), advanced treatment delivery techniques like intensity modulated radiation therapy (IMRT) and volumetric-modulated arc therapy (VMAT) has been proposed (Intensity Modulated Radiation Therapy Collaborative Working Group 2001, Webb 2001, Lehnert 2008, Hall and Giaccia 2012). These treatment delivery techniques highly rely on the sophisticated imaging techniques, such as x-ray computed tomography (CT), magnetic resonance imaging (MRI), and positron emission tomography (PET), to obtain the 3D structural information of the tumor and precisely controlled the radiation beams from different orientations accordingly (Sandler, McLaughlin et al. 1995). However, any uncertainties, including positioning, organ mobility as results of body motion and respiratory motion, and anatomic variations between or during treatment (Xing, Thorndyke et al. 2006, Sterzing, Engenhart-Cabillic et al. 2011), may significantly alter the planned dose delivered to both the malignant tumor and adjacent healthy tissue (Bortfeld, Jokivarsi et al. 2002, Van Herk 2004).

To eliminate these uncertainties and achieve more accurate treatments, image-guided radiation therapy (IGRT) has been introduced as a new concept of radiotherapy, utilizing sophisticated imaging technologies to guide the precise dose delivery in real-time during radiation therapy (Kaus, Netsch et al. 2004, Bucci, Bevan et al. 2005, Ling, Yorke et al. 2006, Li, Citrin et al. 2008, Sterzing, Engenhart-Cabillic et al. 2011). Serval modern imaging techniques has been applied to achieve IGRT (Balter and Cao 2007, Timmerman and Xing 2012, De Los Santos, Popple et al. 2013), including kV planar x-ray, cone-beam CT (Jaffray, Siewerdsen et al. 2002, Goyal and Kataria 2014), EPID (Keall, Todor et al. 2004, Berbeco, Neicu et al. 2005), optical (Bert, Metheany et al. 2005) and ultrasound (US) techniques (Molloy, Chan et al. 2011). However, the imaging methods based on x-ray will bring additional dose to the patients. Optical-based methods, typically video camera monitoring, allow real-time monitoring, but they can only acquire position information about the body surface rather than the internal anatomy. Moreover, all these imaging methods are only focusing on imaging the morphology and motion of the target tissue and lack of the capability in monitoring the radiation beam and its local dose deposition directly.

In previous chapter, we investigated the feasibility of applying XA imaging technique in monitoring dose delivery by clinic Linac during radiation therapy. However, the imaging strategy based-on single element transducer rotational scanning in previous XACT system is time-consuming and lack of practicability in clinic application. Since the XA and US signals from target tissue are both propagating as acoustic waves, XA imaging can be achieved via a US imaging system. Taking the advantages of the state-of-the-art US technologies, the imaging speed of XACT imaging modality can be improved significantly by acquiring data from the parallel ultrasound channels each with commercial-grade receiver sensitivity and noise figures.

Moreover, with the dual-modality arrangement, XA and US images of the imaging target can be scanned using the same system, generally along the same view angle with essentially the same refraction errors, resulting in naturally co-registered images. The US image can present morphologies and motions of the target tissue inside the body, as well as functional information of tumor microenvironments, which are important parameters for treatment planning (Stewart and Li 2007); while the XACT image can determine the spatially distributed dose deposition in the patient body. This combined dual-modality system, which can achieve XA and US imaging simultaneously and in real-time, offers a promising solution to solve the long-standing need for real-time monitoring of beam position and online assessment of delivering dose during radiation therapy.

In this chapter, the viability in real-time monitoring the misalignment of the treatment beam in relation to the target tissue by combining XA imaging technique with established US imaging modality is evaluated. An integrated XACT and B-mode US dual-modality imaging system is established based on a clinically ready research ultrasound platform. Phantom studies are conducted to validate the operability in acquiring XA image and the corresponding US image alternatingly. Its practicability of tracking the relative movement between treatment x-ray beam and the target tissue is demonstrated on phantoms made of biological soft tissue. The issues about weak XA signal and limited spatial resolution are discussed and the possible approaches are evaluated.

6.2 Experimental Setup

The integrated dual-modality imaging system for both XA and B-mode ultrasound imaging is shown in Figure 6-1. With 256 parallel channels, the research ultrasound system (Vantage, Verasonics) can drive two linear array transducer probes (e.g., P4-1, 1-4 MHz, 96 elements, Philips) simultaneously. In the experiment, the two probes are oriented orthogonally both facing the center of the sample that is illuminated by the x-ray beam. The center plane of the target and the scanning planes of the probes were adjusted to the same height which had a source-to-surface distance (SSD) of 100 cm. Probes and phantom are submerged inside water for the coupling of acoustic waves.
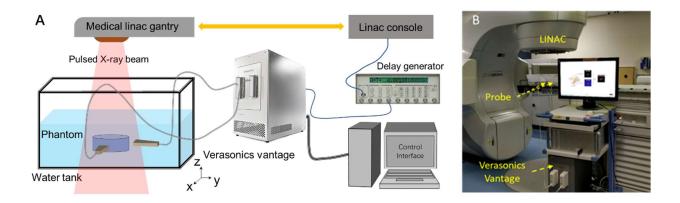
Figure 6-1. (A) Schematic of the XA and B-mode US dual-modality imaging system Verasonics Vantage system. (B) Photograph of the instruments inside the treatment room.

In the XA imaging mode, the clinical radiotherapy Linac (TrueBeam™, Varian Medical systems) shots 6-MV (flattening filter free) photon beam pulses, one of the energy modes used in common clinical radiation therapy practice, from the top with 4 µs pulse duration and 330-Hz repetition rate. The trigger signals from the Linac system, after a delay controlled precisely by a delay generator (SRS DG535, Stanford Research Systems), were sent to the ultrasound system

for synchronization. Since XA SNR was low and, hence, extensive signal averaging was needed, XA signals were acquired continuously for every 15 x-ray pulses until the system switched to the US mode. The XA images were reconstructed and displayed in real time. In the US mode, the probes driven by the same system performed beam steering to achieve B-mode image from the same sample in real time. The B-mode ultrasound mode and the XACT mode ran alternatively, with the time sequence shown in Figure 6-2
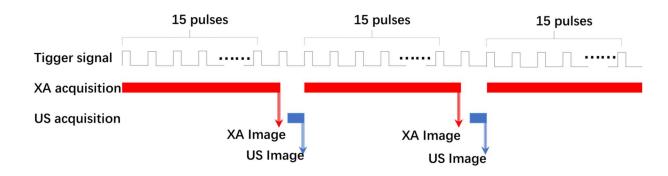
Figure 6-2. Time sequence for XA and B-mode US data acquisition.

In XA signal acquisition process, a time gain control amplifier with up to 40 dB gain was applied to enhance the signal intensity and compensate for the signal attenuation increasing with the depth. An anti-aliasing low-pass filter with 5 MHz cut off frequency was selected to restrict the bandwidth of acquired signals. A 30dB programmable-gain amplifier (PGA) and a 24dB low noise amplifier (LNA) were used to amplify the signal further so that the XA signal intensity can locate in the detectable range of the digitizer. Aiming the low-frequency XA signals, two high pass filters right after the PGA and LNA were disabled to achieve a flat frequency response all the way down to DC. After these analog signal processing, the XA signals were digitized by a 14 bits A/D with 2.5 MHz sampling rate. Due to the low SNR of the acquired XA signals, it was still challenging to reconstruct usable XACT image based on 15 times averaged XA signals. To further enhance the SNR, 2000 times signal averaging was applied before an additional image

reconstruction. Therefore, each frame of such reconstructed XACT image was generated in $2000/(330 \times 15/16) = 6.5$ seconds. For each of the two probes, an XA image was reconstructed using the basic delay-and-sum method. To get the final imaging result, the two images from the two probes were compounded after image co-registration by considering the positions and the orientations of the two probes.

In ultrasound imaging mode, two sets of US image were produced by the two probes under the specific default setting in system for P4-1 transducer probe. The compounding US images were formed after image co-registration between the two probes. Without signal averaging, the B-mode US imaging was conducted with a frame rate of $\frac{330}{16} = 20.6$ Hz. Since the two imaging modalities in our system share the same probes, the XACT and the ultrasound images are naturally co-registered, and can be straightforwardly fused together as a combined image.

6.3 Phantom Studies

6.3.1 Demonstrating the dual-modality imaging capability

To show the capability of the integrated XA and US dual-modality imaging system, a porcine gel (10g/100ml, G2500, Sigma-Aldrich) made cylinder (5 cm in diameter and 3 cm in height) with two lard cylinders (1 cm in diameter and 2 cm in height) embedded was imaged, as shown in Figure 6-3. The x-ray beam was adjusted to a $50\ mm \times 50\ mm$ square shape to cover the whole phantom from top. Following the method described above, XACT and B-mode US images of the phantom were acquired at the same time, reconstructed both in real-time, and displayed simultaneously on the computer screen. Image co-registration was later applied to fuse

the images from the two probes, and then, the two modalities together to generate a combined image showing both the structure and the XA contrast in the phantom.
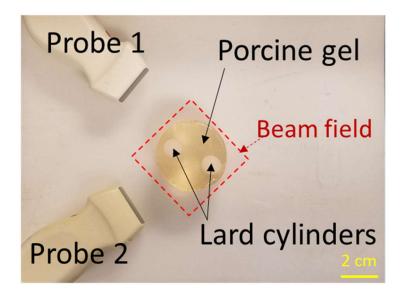
Figure 6-3. Experimental setup for demonstrating dual-modality imaging capability.

The XACT and B-scan US imaging results are shown in Figure 6-4. The normalized gray-scale B-mode ultrasound image shows the structure of the phantom, including the boundary of the porcine gel and the location of the lard cylinders; while the normalized XACT image shows the locations and shapes of the two lard cylinders inside phantom. Here, the XACT images mainly display the contrast due to the Grüneisen parameter difference as discussed in Section 5.3.3.
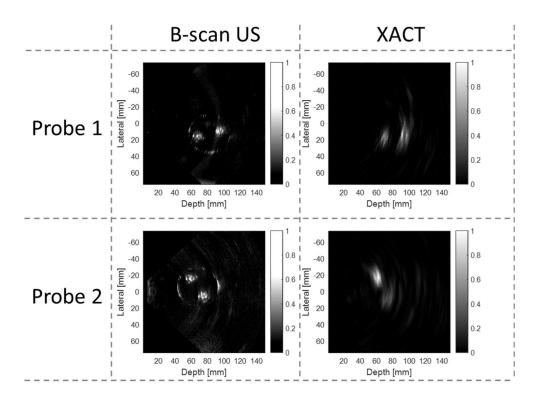
Figure 6-4. The real-time B-scan US and XACT imaging results of the porcine gel phantom containing two lard cylinders.

Images, of either B-scan US or XACT, acquired by two probes can be co-registered based on B-scan US image features and used to form the compounding B-scan US image and compounding XACT image as shown in Figure 6-5 (A) and (B), respectively. Since the B-scan US image and XACT image were acquired under the same coordinate system, they were easily combined together with the B-mode ultrasound presented in gray-scale and the XACT image presented in pseudo-color (red) as shown in Figure 6-5 (C).
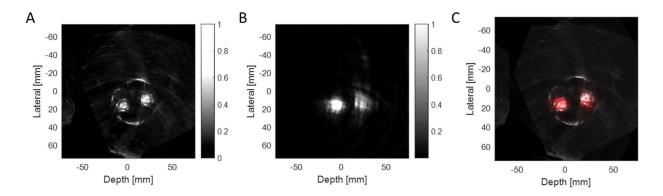
Figure 6-5. Compounding B-scan US images (A) and XACT images (B). B-scan US and XACT combined image.

6.3.2 Tracking the x-ray beam position

Comparing with showing the contrast due to different Grüneisen parameters, showing the x-ray beam position will be a much more essential feature for our system. To verify the performance of the system in tracking the positions of the x-ray beam, a lard cuboid $(5 \times 5 \times 2 cm^3)$ was embedded in a porcine gel block. In this part of study, only one probe was applied for imaging. The x-ray beam with a size of $10mm \times 10mm$ shot the phantom vertically from above. After each XACT image was taken, beam was repositioned to next location through moving the jaws inside gantry controlled the Linac consoler. As illustrated in Figure 6-6, the x-ray beam on the sample was moved away from the original position, first along the x-axis for 3 steps with a constant step size of 3 mm and then along the y-axis for 1 more step with a step size of 6 mm. For each location of the x-ray beam, an XACT image of the phantom was acquired.
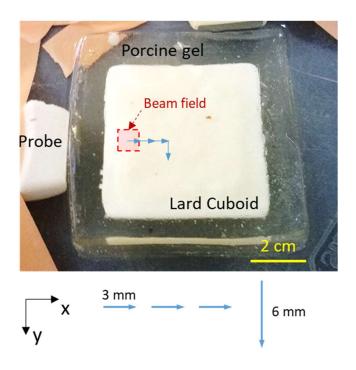
Figure 6-6. Experimental setup for validating the capability of the system in tracking beam position.

The XACT images in Figure 6-7 show the spatial distribution of dose deposition in the sample at different locations before and after the beam repositioned. The original beam location is marked by the red dashed square. As we can see in the images after the beam repositioning, the x-ray energy deposition in the sample changed accordingly. The location of the beam in each image was marked by a dashed square with different colors (red, green, orange, blue, and yellow). By quantifying the distance between each square to the original square in red, we determined the movement distances after the beam repositioning based on their central points, which were (2.5, -0.3) mm, (5.8, -0.3) mm, (8.5, 0.3) mm, and (8.7, 6.3) mm, respectively, matching with the programmed moving path of the x-ray beam (i.e., (3.0, 0) mm, (6.0, 0) mm, (9.0, 0) mm, and (9.0, 6.0) mm). This result demonstrated that the position of the delivered x-ray beam in the sample could be mapped by XACT with good accuracy.

94
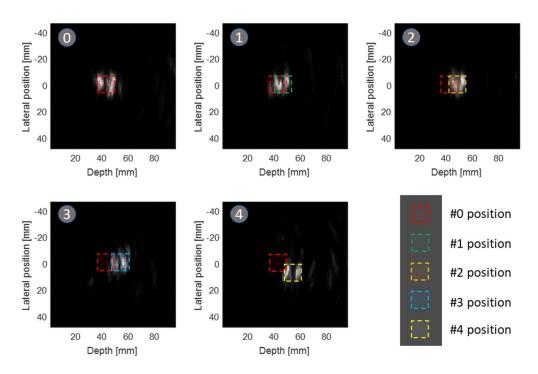
Figure 6-7. XACT imaging results show the x-ray beam at different locations on the lard cuboid. The different locations of the delivered x-ray beam, from #0 to #5, are marked by the dashed squares (red, green, orange, blue, and yellow, respectively).

6.3.3 Monitoring the misalignment of beam in relation to target due to tissue motion

To verify the performance of the system in tracking the movement of the target tissue with respect to the position of the treatment beam, both XACT and ultrasound imaging of a phantom were conducted simultaneously in this part of experiment. The phantom was a block of pork belly embedded in porcine gel. To make an artificial tumor in the phantom, a hole with a size of $1 \times 1 \times 2.5 \ cm^3$ was cut in the pork belly which was filled with fatty tissue and then covered by a thin layer of muscle. This artificial tumor can offer an acoustic boundary so that it can be captured in ultrasound imaging. The photographs of the experimental setup are shown in Figure 6-8. The movement of the phantom was precisely driven by two stepper motors, first along the x-axis for 3 steps with a constant step size of $5 \ mm$ and then along the y-axis for two steps with a

constant step size of $-5\ mm$. Initially before any movement, the x-ray beam with a size of $10\ mm \times 10\ mm$ was aligned to shot the phantom vertically from above and cover the entire artificial tumor. When the phantom was moved and the x-ray beam position was kept static, the x-ray beam started to misalign with the target tumor. Before and after each movement of the phantom, both XACT and ultrasound images of the phantom were acquired.
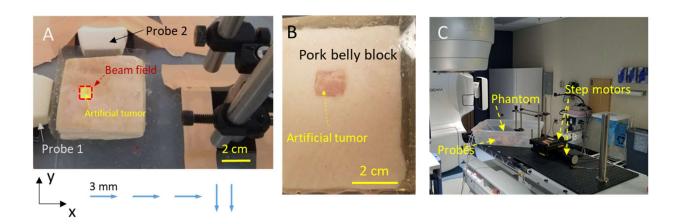
Figure 6-8. (A) The experimental setup for validating the capability of the system in monitoring the misalignment of treatment beam in relation to the target tissue. The instruments inside the treatment room (B) The bottom view of the phantom with the position of the artificial tumor. (C) Photography for the setups inside the treatment room.

Figure 6-9 shows the imaging result demonstrating the capability of our XACT and ultrasound dual-modality imaging system in tracking the tissue movement with respect to the location of the X-ray beam. In each combined image, the ultrasound image in gray-scale shows the tissue structure including the position of the artificial tumor. The changes in location of the artificial tumor as a result of the phantom movement can be captured, and also matched well with the programmed movement steps. The XACT image in pseudo-color shows the location of the x-ray dose deposition in the target tissue, as marked by the red dashed box, which was kept

static in this experiment. As shown in Figure 6-9 (A), initially the x-ray beam aligned well with the target. Then, due to the tissue movement, the x-ray beam was gradually away from the target.
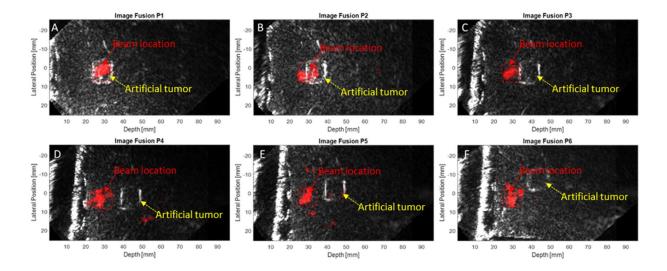
Figure 6-9. XACT and ultrasound dual-modality imaging for tracking of tissue movement in respect to the x-ray beam. In each combined image, the XACT image in pseudo-color presenting the location of the beam is superimposed on the ultrasound image in gray-scale showing the tissue structure. (A) The combined image acquired when x-ray beam was alignment with the target artificial tumor. (B-F) The combined images acquired after the tissue movements.

6.4 Approaches to Improve XACT Image Quality

6.4.1 Weak signal

In the experiments, we have utilized the lipid or fat tissue with high Grüneisen parameter so that the phantom can achieve detectable XA signals for x-ray beam. The XA signal from other kinds of tissue may not be strong enough to be acquired by our current system due to the limited detection sensitivity of the commercial ultrasound unit. Figure 6-10 shows the digitized XA signal acquired during the experiment in Section 6.3.2 before and after 2000 times averaging.

The XA signal strength is almost closed to the Dead-band of the digitization. In order to increase the intensity of XA signal before it is sent to A/D converter, several potential solutions can be considered.
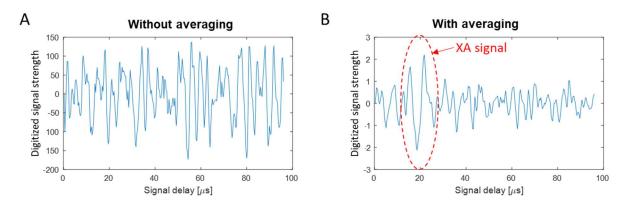
Figure 6-10. Example of digitized XA signals acquired from a single channel without (A) and with (B) 2000 times averaging.

The main lobe of the frequency spectrum of the XA signal produced by the current Linac is around 250 kHz due to the 4 μs pulse duration of the x-ray source. However, currently applied P4-1 probe, which is one of the lowest frequency probes that are commercially available, still cannot cover this very low-frequency range of the XA signals. To improve the detection sensitivity, customer-designed transducer probe working at lower frequency should be employed. Besides providing a matching detection frequency, the probes working at lower frequency will also have larger element sizes which will also improve the detection sensitivity.

On the other hand, the dynamic range of the currently employed Verasonics US unit does not match with the intensity scale of the XA signal produced. Therefore, the XA signal acquired by the transducer probe should be further amplified before feeding to the A/D converter of the US platform. As all the built-in amplifiers in the US platform are already maximized, an extra multi-channel preamplifier board is needed.

Considering the limited dynamic range of the 14 bits A/D in the Verasonics US platform, the maximum amplification can be applied before saturating the noises is about 38dB. A customized 128-channel low-noise preamplifier board (38 dB, 60 kHz ~12 MHz, PhotoSound Technologies, Houston, Texas) has been developed and applied between the probe and the US platform. Figure 6-11 shows the digitized XA signal acquired from a lard phantom shot by 20 mm × 20 mm 6-MV (flattening filter free) x-ray beam before and after 2000 times averaging. Even though the SNR is not changed, the range of XA is pulled away from the Dead-band, which makes it possible to capture weaker signals and preserve the details of XA signal during the digitizing process. Figure 6-12 shows the XACT images acquired from water shot by a 10 MV (flattening filter free) x-ray beam with a size of 20 mm × 20 mm. With the amplification, the two boundaries of the beam perpendicular to the probe can be observed in the XACT image.
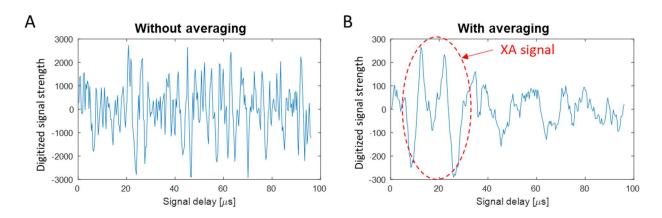
Figure 6-11. Example of digitized XA signals applied preamplifier board
without (A) and with (B) 2000 times averaging.
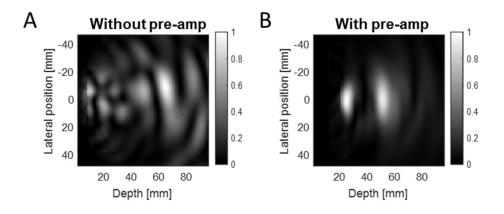
Figure 6-12. Normalized XACT images for $20\ mm \times 20\ mm$ x-ray beam on water without (A) and with (B) preamplifier board.

6.4.2 Low spatial resolution

Due to the pulse duration of the x-ray source, which was about 4 μs, a low-frequency detection probe was applied to ensure the signal strength. Hence, the axial resolution of the reconstructed XACT image was about 6 mm. The lateral resolution is limited by both the frequency and the numerical aperture of the transducer probe. Allowed by the 256 parallel channels of the Verasonics US platform, two P4-1 probes can be used simultaneously. With the two probes oriented orthogonally, the lateral resolution is essentially dependent on the axial resolution. Therefore, the spatial resolution system demonstrated in Section 6.3.1 is basically limited by the x-ray pulse duration, which can be reduced only via the collaboration with the manufactures of the Linac systems. Another possible solution to improve the spatial resolution of XACT is to perform a deconvolution, which could partially remove the effect of the long x-ray pulse duration. As shown in eq. (2-17), the normalized temporal profile of the radiation pulse $h_t(t)$ can be treated as an impulse response convoluting with the rest terms. So the induced signal $p(t)$ can be written as (Yi, Da et al. 2004):

$$p(t) = \frac{1}{4\pi v_s^2} \left(\frac{1}{t} \iint d\theta d\varphi \sin\theta \, (tv_s)^2 p_0(tv_s, \theta, \varphi) h_s(tv_s, \theta, \varphi) \right) * \frac{dh_t(t)}{dt}. \qquad \text{6-1}$$

By removing the term $\frac{dh_t(t)}{dt}$ through a deconvolution process, the left terms noted as $p_{de}(t)$

will be the acoustic pressure induced by a perfect short radiation pulse.

To test the practicability of this deconvolution approach in XACT imaging, four lead sheets

with different thickness were used as the imaging targets to test the potential spatial resolution.

As shown in Figure 6-13 (A - D), the lead sheets have 3 cm in length and 2 cm in height, with

different thicknesses of 1 mm, 1.5 mm, 3 mm and 4.5 mm, respectively. Before imaging, each

lead sheet was embedded in a porcine gel block and was put 2 cm away from the probe, as

shown in Figure 6-13. The porcine gel block and the probe were submerged inside water during

the measurement. In this experiment, each lead sheet was imaged by only one probe.
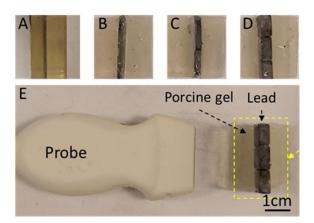
Figure 6-13. Photographs of four lead sheets used for testing the spatial
resolution of XACT imaging. (A - D) The thicknesses of the four lead sheets
were 1 mm, 1.5 mm, 3 mm, and 4.5 mm, respectively. (E) Experimental setup
for XACT imaging of individual lead sheet.

The temporal profile of the x-ray pulse $h_t(t)$ was acquired indirectly. The target signal

from the Linac consoler we used as trigger signal offers the voltage signal due to the high energy

colliding the heavy metal target for producing photons. Hence, the captured target signal (shown in Figure 6-14 [A]) was applied as an alternative. The derivative of the target signal profile is plotted with its power spectrum in Figure 6-14 (B). As shown in Figure 6-14 (C), the A-line XA signal acquired by one of probe elements for 1.5 mm lead sheet contained two peaks: a positive one and a negative one with a delay of about 4 μs between. Since the US probe applied was not covering the low-frequency range, typically the 250 kHz corresponding to the pulse duration, most of the XA signals acquired were around the 2.25 MHz central frequency of the probe. In this case, the rising and failing edges of a single x-ray pulse generated two independent XA signals (i.e., the positive peak and the negative peak in Figure 6-14 [C]). By performing deconvolution, only one peak left in the A-line XA signal as shown in Figure 6-14 (D).
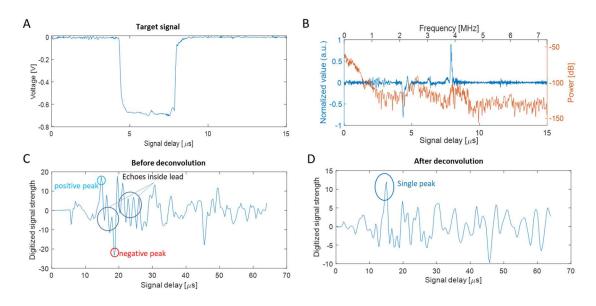
Figure 6-14. (A) Target signal from the Linac consoler showing the temporal profile. (B) The derivative of the temporal profile in (A) and its power spectrum. The frequency spectrum of the x-ray pulse. A-line XA signal generated on a 1.5-mm lead sheet and acquired by one of the probe elements before (C) and after (D) deconvolution.

The XACT images of the lead sheets with thicknesses of 1 mm, 1.5 mm, 3 mm, and 4.5 mm, before and after deconvolution are shown in Figure 6-15. The intensity profiles along the dotted lines in images with deconvolution are presented in Figure 6-16 (A), where all the profiles were normalized. The quantified full width at half maximum (FWHM) of the four intensity profiles are 1.3 mm, 1.7 mm, 3.6 mm, and 4.9 mm, respectively, for the four lead sheets, as shown in Figure 6-16 (B). The results suggest that the improved spatial resolution of the current XACT system is better than 1.3 mm. Typically, this value should be bounded by the frequency components of x-ray pulse profile, especially the frequency corresponding to the rising and failing time (Gao, Feng et al. 2017). The bandwidth of the acquisition system may further degrade the spatial resolution.
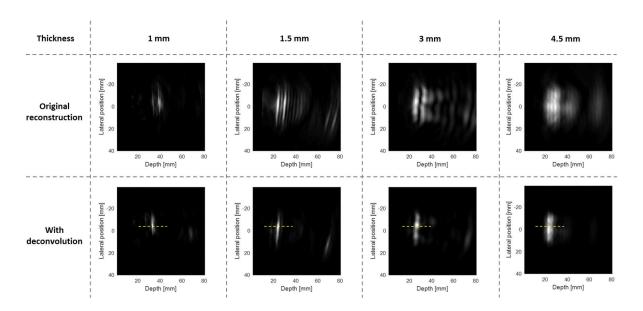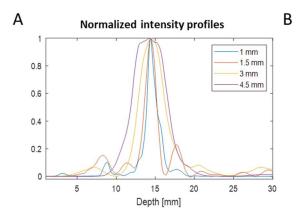
Figure 6-15. The XACT images of lead sheets with various thicknesses, before and after applying deconvolution.

103

Normalized intensity profiles

Thickness of lead sheets	FWHM of intensity profiles
1.0 mm	1.3 mm
1.5 mm	1.7 mm
3.0 mm	3.6 mm
4.5 mm	4.9 mm

Figure 6-16. (A) Normalized intensity profiles along the dotted lines in Figure 6-15. (B) FWHM of the normalized intensity profiles in (A).

6.5 Discussion

Building XA and US dual-modality imaging by utilizing a commercial US unit can largely accelerate the technology development and benefit the possible translation to clinic. Using the same ultrasound probe driven by a large number of parallel channels of the US unit for detection of XACT signals not only improves the imaging speed but also facilitate a natural co-registration between the XACT image mapping the dose deposition and the ultrasound image rendering the tissue structure. Despite these advantages, XACT built on the commercial US unit, however, suffers from the limited detection sensitivity. Although our initial experimental results demonstrated that XACT could be realized through a commercially available US system, to achieve sufficient SNR for imaging of soft-tissue samples, extensive signal averaging was required, which inevitably reduced the imaging speed. As shown by this study, the frame rate of the dual-modality imaging is over 20 Hz for B-mode ultrasound but only 0.15 Hz for XACT which is limited by the extensive signal averaging over 2,000 times. The weak signal strength of acquired XA signal is also a part of the reason that the current XACT image quality is not ideal,

as reflected by strong artifacts and low contrast-to-noise ratio. As a solution, we applied a multi-channel low-noise preamplifier board so that the weak XACT signals can be initially amplified before they are processed by the US unit. According to the test with the preamplifier, although SNR was not significantly improved, the quantization error was reduced as the analog signal was increased before the digitization. Therefore, further improvement in the future may focus decreasing system noise, increasing system dynamic range, and improving low-frequency response of the transducer probe.

Another limitation of the XACT realized by the current system is its relatively low spatial resolution, which is mainly caused by the 4 μs pulse duration of the x-ray source. As a result, the produced XA signals are more dominated at the very low-frequency range around 200 kHz. To better detect these low-frequency signals, a P4-1 probe, which is one of the lowest frequency probes that are commercially available, was applied. However, the P4-1 probe still cannot cover the very low-frequency range of the XA signals. Deconvolution was tested as a potential method to remove the effect of the long x-ray pulse duration. This method, however, may turn out to be difficult to use especially when the probe for XACT has limited bandwidth. In the future, when the x-ray pulse duration from the Linac system could be further reduced, the XA signal in the tissue can be generated with not only higher efficiency but also higher frequency and broader bandwidth. Then a probe working at a higher frequency with broader bandwidth can be employed to improve the spatial resolution of XACT.

6.6 Conclusion

In this Chapter, an XA and US dual-modality imaging system was developed on a clinically ready research ultrasound platform. Taking advantages from the large number of parallel channels and the excellent controllability of the research ultrasound platform, XACT and B-scan ultrasound of soft-tissue samples can be achieved simultaneously and in real time. Its feasibilities in mapping the x-ray dose in soft-tissue phantoms and its capability in monitoring the alignment of the x-ray beam in respect to the target tissue were investigated. This technology, although at its early stage of development, renders a promising method for IGRT that can achieve imaging of the tissue morphology and mapping of radiation dose deposition simultaneously, both in real-time fashion.

Chapter 7

Conclusions and Future Work

7.1 Conclusions

This research investigated thermoacoustic (TA) imaging techniques in (1) characterizing the intestinal strictures of Crohn's disease *in vivo* by quantifying relevant histochemical components inside the bowel wall non-invasively with photoacoustic (PA) imaging technique, and (2) monitoring the performance of dose delivery during radiation therapy conducted by Linac towards achieving *in vivo* dosimetry and image-guided radiotherapy based on x-ray induced acoustic (XA) imaging technique.

7.1.1 Photoacoustic imaging developments

In this part of research, we applied PA imaging technique to improve the diagnosis of Crohn's disease, especially solving the challenge of characterizing the intestinal strictures in bowel. We validated the feasibility of assessing the spatially varying molecular components in ex vivo intestinal strictures by obtaining PA molecular component images using a developed acoustic resolution PA microscopy (AR-PAM) system. Then, we miniaturized the AR-PAM to a prototype side-view scanning capsule-shaped probe and proved its practicability in quantitatively differentiate the intestinal disease conditions by performing *in vivo* colonoscopy in the rabbit disease model. In the future, an endoscopic AR-PAM combined with PA molecular component

imaging method could be an operational strategy for characterizing the intestinal strictures of Crohn's disease (CD) *in vivo*.

This is the first study that implemented PA imaging for the diagnosis of intestinal strictures in Crohn's disease. As mentioned in the previous chapters, currently no diagnostic modality can identify intestinal fibrosis. The developed imaging probe approach fits seamlessly to the existing diagnostic and therapeutic colonoscopy procedures and provides more specific diagnostic information. Further miniaturization of the probe allowing the retraction of the probe and insertion of other device through the instrument channel.

The major contributions in this part of research are:

- A prototype AR-PAM system was developed and achieved multiwavelength PA scans on *ex vivo* tissues non-invasively. The method for obtaining the PA molecular component images was established based on multiwavelength PA intensity images acquired by the proposed AR-PAM system. The feasibility of assessing the spatially varying molecular components in intestinal strictures via the AR-PAM system was validated through *ex vivo* tissues from human subjects affected by CD.

- A prototype capsule-shaped AR-PAM probe was further developed to enable side-view scanning of the bowel wall to produce PA molecular component images. Motion artifacts caused by intestinal peristalsis were compensated for to improve image quality. The problem of limited depth of view caused by the highly focusing transducer was resolved. The capability of the probe to quantitatively differentiate the intestinal disease conditions of Crohn's disease was validated in a rabbit model *in vivo*. The feasibility of monitoring the development of fibrosis in early and

refractory conditions were investigated by longitudinal measurements on rabbits.

7.1.2 X-ray acoustic imaging applications

In this part of research, we evaluated the potential applications of XA imaging technique. Based on soft-tissue phantom studies, its feasibility in monitoring the position of the x-ray beam and measuring the spatially varying dose deposition was validated. These results suggested a potential application of XA imaging method, specifically XACT, as a novel *in vivo* dosimetric tool in external beam radiotherapy (EBRT). After validating the feasibility of XACT, we further developed an XA and US dual-modality imaging system utilizing a commercial ultrasound unit, aiming to obtain XA image and US image simultaneously, both in real time. As demonstrated by the experiments on soft-tissue phantoms, the XA image showing the deposited radiation dose and the US image capturing the motion of target tissue can be naturally co-registered, offering a potential approach for image-guided radiotherapy (IGRT).

The major contributions in this part of research are:

- A prototype XACT system based on the scanning of a single transducer was established to achieve XA imaging on phantoms made of soft biological tissue. The possible imaging contrasts and acquisition of XACT images were evaluated. The feasibility of measuring accurate dose deposition based on XACT images was validated in soft-tissue phantom studies. The potential of XACT to track the position of the dose delivery and measure beam–target misalignments was demonstrated.

- An XA and US dual-modality imaging system was developed on a clinically ready research ultrasound platform, where XACT and B-scan ultrasound of soft-tissue

samples could be achieved simultaneously and in real time. The feasibility in mapping the x-ray dose in soft-tissue phantoms was validated. Its capability in monitoring the relative movement of the x-ray beam with respect to the target due to tissue motion was investigated. The potential solutions for the problems of weak XA signal and low spatial resolution were also initially evaluated.

7.2 Future Work

Due to the limited penetration of light and US wave, the PA probe must be positioned close to the region of interest by the method of endoscopy. However, due to the limited space inside the endoscopic probe, improving the imaging quality and imaging depth are still challenging. Two future research directions following the studies in this dissertation are suggested:

- As we need to compensate the light fluence distribution due to the high attenuation, the simulated result at 1310 nm showed the light fluence at the depth of 7 mm may be only 1/100 of the light fluence near the tissue surface. Even though the signal strength can be compensated, the difference in signal-to-noise-ratio (SNR) will remain and the partial of the dynamic region for the acquisition system must be occupied. For detecting the endogenous biomarkers such as lipids and collagen which have relative low contrast, a high light fluence at tissue surface is required to preserve strong enough light fluence at the deep region for an adequate SNR. This problem is not that significant in this work because the rabbit has much thinner bowel wall

comparing with the intestinal structure of human. To transfer the application of the PA probe to human intestinal examination, an improved light projection will be necessary to offer either stronger light delivery or induce a gentle light fluence decay inside the tissue. Currently, the light energy that can be guided into the probe through fiber is limited. Therefore, exogenous contrast agents which can target specific molecule or cells may be the alternative solution.

- In the acoustic part, a digital refocusing method was applied in Section 4.3.2 to overcome the conflict between the demands of high lateral resolution and large depth-of-field. However, this digital processing, as a virtual aperture reconstruction method, is sensitive to the motion artifacts. In this work, we simply did the digital refocusing after the motion artifacts compensation. It should be worth to combine the two processes for more comprehensive image reconstruction. Beside the digital processing solution, any mechanical or phased scan on transducer could be applied. The endoscopic probe has a strong constraint in its radial dimension, but it always has enough room in the axial direction. With the help of an acoustic reflector, scanning in the radial direction can be achieved through the motion in the axial direction. Meanwhile, instead of using a fixed focusing transducer, applying an annular array or phased array will simplify the mechanical scanning process and achieve the adjustable focusing easily.

In this dissertation, the applications of XA imaging technique in monitoring x-ray dose deposition as a dosimetric tool and a potential solution for image-guided radiotherapy (IGRT) were evaluated and investigated. As discussed in the corresponding sections, there

are several research objectives that are necessary in the future before this technology can be adapted to clinic settings:

- According to the necessities of the dosimetric application, the acquired XA images should keep quantitative in a scale up to several centimeters, which is corresponding to a very low frequency about tens of kilohertz. At the same time, the XA images are also required to have an excellent spatial resolution, which is related to a high-frequency range around several megahertz. The gap between these two frequency bands makes it quite challenging to achieve ideal XA images for dosimetry. One possible solution is to scarify the low-frequency components and focusing on the frequency range around 3 MHz corresponding to the temporal profile of the x-ray pulse as shown in Figure 6-14 (B), which will offer both workable SNR and spatial resolution. Due to the loss of low-frequency component, however, the XA images will suffer strongly from the edge enhancement effects. Fortunately, different from other imagine applications, most of the features inside XA images are already known, for example the exact shape of the x-ray beam. This kind of information should be helpful in compensating for the edge enhancement effect due to the missing of the low frequency signal. Another possible solution may be acquiring XA signal using multiple (e.g., two) probes working at different frequency bands. The low-frequency range down to tens of kilohertz covered by the low-frequency probe could form the fundamental shape of the x-ray dose deposition, while the high-frequency range up to 3MHz covered by the high-frequency probe could be utilized to bring details and sharpness of the

boundaries. One benefit of this strategy is that the problem of weak signal and low SNR will be dramatically reduced once the low-frequency component is covered.

- Even though the feasibility of XA imaging in measuring the dose delivered by treatment beam was validated based on the XACT system with single element transducer, dose measurement is still challenging for the case of acquire XA image with the phased US array. Based on the XA and US dual-modality system established in Chapter 6, we can only acquire the shapes and positions of the x-ray beam due to the low SNR and weak signal. As the amplification board involved at the end of acquisition is almost saturating the noise, further improvement should rely on improving the sensitivity of the phased transducer array and reducing the noise of the system. However, as discussed above, enhancing the sensitivity of the transducer may lead to a decrease in spatial resolution or a complex sensor system. On the other side of the coin, working with a linac with shorter x-ray pulse duration will be the utmost solution if possible.

- According to eq. (5-3), the spatially varying thermal efficiency, Grüneisen parameter, and mass density will also contribute to the XA signal strength, independent from the dose deposition. The map of the mass density may be easy to obtain through the x-ray CT during the treatment planning. The main contribution to the difference in Grüneisen parameter is the ratio between lipids and water, which may be determined by MRI (Hu, Li et al. 2011) or x-ray CT (Johns and Yaffe 1987).

BIBLIOGRAPHY

Achkar, E., W. D. Carey, R. Petras, M. V. Sivak and R. Revta (1986). "Comparison of suction capsule and endoscopic biopsy of small bowel mucosa." Gastrointestinal Endoscopy **32**(4): 278-281.

Aliroteh, M., H. Nan and A. Arbabian (2016). Microwave-induced Thermoacoustic tomography for subcutaneous vascular imaging. 2016 IEEE International Ultrasonics Symposium (IUS).

American National Standards Institute (2007). American national standard for safe use of lasers, Laser Institute of America.

Balter, J. M. and Y. Cao (2007). Advanced technologies in image-guided radiation therapy. Seminars in Radiation Oncology, Elsevier.

Bell, A. G. (1880). "The photophone." Science **1**(11): 130-134.

Berbeco, R. I., T. Neicu, E. Rietzel, G. T. Chen and S. B. Jiang (2005). "A technique for respiratory-gated radiotherapy treatment verification with an EPID in cine mode." Physics in Medicine & Biology **50**(16): 3669.

Bert, C., K. G. Metheany, K. Doppke and G. T. Chen (2005). "A phantom evaluation of a stereo-vision surface imaging system for radiotherapy patient setup." Medical physics **32**(9): 2753-2762.

Bortfeld, T., K. Jokivarsi, M. Goitein, J. Kung and S. B. Jiang (2002). "Effects of intra-fraction motion on IMRT dose delivery: statistical analysis and simulation." Physics in Medicine & Biology **47**(13): 2203.

Boudiaf, M., P. Soyer, C. Terem, J. P. Pelage, E. Maissiat and R. Rymer (2001). "CT Evaluation of Small Bowel Obstruction." RadioGraphics **21**(3): 613-624.

Bowen, T. (1981). Radiation-Induced Thermoacoustic Soft Tissue Imaging. 1981 Ultrasonics Symposium.

Bowen, T., C. X. Chen, S. C. Liew, W. R. Lutz and R. L. Nasoni (1991). "Observation of ultrasonic emission from edges of therapeutic X-ray beams." Physics in Medicine & Biology **36**(4): 537.

Bucci, M. K., A. Bevan and M. Roach (2005). "Advances in radiation therapy: conventional to 3D, to IMRT, to 4D, and beyond." CA: a cancer journal for clinicians **55**(2): 117-134.

Cai, D., Z. Li and S.-L. Chen (2016). "In vivo deconvolution acoustic-resolution photoacoustic microscopy in three dimensions." <u>Biomedical Optics Express</u> **7**(2): 369-380.

Cai, D., Z. Li, Y. Li, Z. Guo and S.-L. Chen (2017). "Photoacoustic microscopy in vivo using synthetic-aperture focusing technique combined with three-dimensional deconvolution." <u>Optics Express</u> **25**(2): 1421-1434.

Chen, J., R. Lin, H. Wang, J. Meng, H. Zheng and L. Song (2013). "Blind-deconvolution optical-resolution photoacoustic microscopy in vivo." <u>Optics Express</u> **21**(6): 7316-7327.

Cheong, W. F., S. A. Prahl and A. J. Welch (1990). "A review of the optical properties of biological tissues." <u>Quantum Electronics, IEEE Journal of</u> **26**(12): 2166-2185.

Chiorean, L., D. Schreiber-Dietrich, B. Braden, X. Cui and C. F. Dietrich (2014). "Transabdominal ultrasound for standardized measurement of bowel wall thickness in normal children and those with Crohn's disease." <u>Medical ultrasonography</u> **16**(4): 319-324.

Chuang, C. F., L. J. Verhey and P. Xia (2002). "Investigation of the use of MOSFET for clinical IMRT dosimetric verification." <u>Medical physics</u> **29**(6): 1109-1115.

Cohen, R. D., L. R. Larson, J. M. Roth, R. V. Becker and L. L. Mummert (2000). "The cost of hospitalization in Crohn's disease." <u>Am J Gastroenterol</u> **95**(2): 524-530.

Cox, B., J. G. Laufer, S. R. Arridge and P. C. Beard (2012). "Quantitative spectroscopic photoacoustic imaging: a review." <u>Journal of Biomedical Optics</u> **17**(6): 061202-061201.

Cox, B. T., S. R. Arridge, K. P. Köstli and P. C. Beard (2006). "Two-dimensional quantitative photoacoustic image reconstruction of absorption distributions in scattering media by use of a simple iterative method." <u>Appl. Opt.</u> **45**(8): 1866-1875.

Cox, B. T., J. G. Laufer and P. C. Beard (2009). <u>The challenges for quantitative photoacoustic imaging</u>. SPIE BiOS, SPIE.

Dandalides, S., W. Carey, R. Petras and E. Achkar (1989). "Endoscopic small bowel mucosal biopsy: a controlled trial evaluating forceps size and biopsy location in the diagnosis of normal and abnormal mucosal architecture." <u>Gastrointestinal Endoscopy</u> **35**(3): 197-200.

De La Zerda, A., C. Zavaleta, S. Keren, S. Vaithilingam, S. Bodapati, Z. Liu, J. Levi, B. R. Smith, T.-J. Ma and O. Oralkan (2008). "Carbon nanotubes as photoacoustic molecular imaging agents in living mice." <u>Nature nanotechnology</u> **3**(9): 557.

De Los Santos, J., R. Popple, N. Agazaryan, J. E. Bayouth, J.-P. Bissonnette, M. K. Bucci, S. Dieterich, L. Dong, K. M. Forster and D. Indelicato (2013). "Image guided radiation therapy (IGRT) technologies for radiation therapy localization and delivery." <u>International Journal of Radiation Oncology* Biology* Physics</u> **87**(1): 33-45.

Deng, Z., X. Yang, H. Gong and Q. Luo (2011). "Two-dimensional synthetic-aperture focusing technique in photoacoustic microscopy." <u>Journal of Applied Physics</u> **109**(10): 104701.

Dillman, J. R., R. W. Stidham, P. D. Higgins, D. S. Moons, L. A. Johnson and J. M. Rubin (2013). "US elastography-derived shear wave velocity helps distinguish acutely inflamed from fibrotic bowel in a Crohn disease animal model." Radiology **267**(3): 757-766.

Dillman, J. R., S. D. Swanson, L. A. Johnson, D. S. Moons, J. Adler, R. W. Stidham and P. D. Higgins (2014). "Comparison of noncontrast MRI magnetization transfer and T -Weighted signal intensity ratios for detection of bowel wall fibrosis in a Crohn's disease animal model." J Magn Reson Imaging.

Domènech, E., M. Mañosa and E. Cabré (2009). "Top-Down Therapy: Is the Evidence Strong Enough?" Digestive Diseases **27**(3): 306-311.

Eliakim, R., Z. Fireman, I. Gralnek, K. Yassin, M. Waterman, Y. Kopelman, J. Lachter, B. Koslowsky and S. Adler (2006). "Evaluation of the PillCam Colon capsule in the detection of colonic pathology: results of the first multicenter, prospective, comparative study." Endoscopy **38**(10): 963-970.

Erpelding, T. N., C. Kim, M. Pramanik, L. Jankovic, K. Maslov, Z. Guo, J. A. Margenthaler, M. D. Pashley and L. V. Wang (2010). "Sentinel Lymph Nodes in the Rat: Noninvasive Photoacoustic and US Imaging with a Clinical US System." Radiology **256**(1): 102-110.

Foster, F. S., G. R. Lockwood, L. K. Ryan, K. A. Harasiewicz, L. Berube and A. M. Rauth (1993). "Principles and applications of ultrasound backscatter microscopy." IEEE Transactions on Ultrasonics, Ferroelectrics, and Frequency Control **40**(5): 608-617.

Gao, F., X. Feng, R. Zhang, S. Liu, R. Ding, R. Kishor and Y. Zheng (2017). "Single laser pulse generates dual photoacoustic signals for differential contrast photoacoustic imaging." Scientific Reports **7**(1): 626.

Glaser, A. K., R. Zhang, D. J. Gladstone, B. W. J. P. i. M. Pogue and Biology (2014). "Optical dosimetry of radiotherapy beams using Cherenkov radiation: the relationship between light emission and dose." **59**(14): 3789.

Goyal, S. and T. Kataria (2014). "Image guidance in radiation therapy: techniques and applications." Radiology research and practice **2014**.

Graham, M. F., R. F. Diegelmann, C. O. Elson, W. J. Lindblad, N. Gotschalk, S. Gay and R. Gay (1988). "Collagen content and types in the intestinal strictures of Crohn's disease." Gastroenterology **94**(2): 257-265.

Gunderson, L. L. (2015). Clinical radiation oncology, Elsevier Health Sciences.

Guo, Z., L. Li and L. V. Wang (2009). "On the speckle-free nature of photoacoustic tomography." Medical physics **36**(9Part1): 4084-4088.

Hall, E. J. and A. J. Giaccia (2012). Radiobiology for the radiologist. Philadelphia, Wolters Kluwer Health/Lippincott Williams & Wilkins.

Hickling, S., P. Léger and I. El Naqa (2016). "On the detectability of acoustic waves induced following irradiation by a radiotherapy linear accelerator." IEEE transactions on ultrasonics, ferroelectrics, and frequency control **63**(5): 683-690.

Hickling, S., H. Lei, M. Hobson, P. Léger, X. Wang and I. El Naqa (2017). "Experimental evaluation of x-ray acoustic computed tomography for radiotherapy dosimetry applications." Medical Physics **44**(2): 608-617.

Hoelen, C. G. A. and F. F. M. d. Mul (1999). "A new theoretical approach to photoacoustic signal generation." The Journal of the Acoustical Society of America **106**(2): 695-706.

Hollman, K. W., K. W. Rigby and M. O. Donnell (1999). Coherence factor of speckle from a multi-row probe. 1999 IEEE Ultrasonics Symposium. Proceedings. International Symposium (Cat. No.99CH37027).

Hu, H. H., Y. Li, T. R. Nagy, M. I. Goran and K. S. Nayak (2011). "Quantification of Absolute Fat Mass by Magnetic Resonance Imaging: a Validation Study against Chemical Analysis." International journal of body composition research **9**(3): 111-122.

Hubbell, J. H. and S. M. Seltzer (1995). Tables of X-ray mass attenuation coefficients and mass energy-absorption coefficients 1 keV to 20 MeV for elements Z= 1 to 92 and 48 additional substances of dosimetric interest, National Inst. of Standards and Technology-PL, Gaithersburg, MD (United States). Ionizing Radiation Div.

Huyskens, D. P. (2001). Practical Guidelines for the Implementation of in Vivo Dosimetry with Diodes in External Radiotherapy with Photon Beams (entrance Dose), ESTRO.

Intensity Modulated Radiation Therapy Collaborative Working Group (2001). "Intensity-modulated radiotherapy: current status and issues of interest." International Journal of Radiation Oncology* Biology* Physics **51**(4): 880-914.

Jaffray, D. A., J. H. Siewerdsen, J. W. Wong and A. A. Martinez (2002). "Flat-panel cone-beam computed tomography for image-guided radiation therapy." International Journal of Radiation Oncology* Biology* Physics **53**(5): 1337-1349.

Johns, P. C. and M. Yaffe (1987). "X-ray characterisation of normal and neoplastic breast tissues." Physics in Medicine & Biology **32**(6): 675.

Jones, D. W. and S. R. G. Finlayson (2010). "Trends in Surgery for Crohn's Disease in the Era of Infliximab." Annals of Surgery **252**(2): 307-312 310.1097/SLA.1090b1013e3181e1061df1095.

Jornet, N., P. Carrasco, D. Jurado, A. Ruiz, T. Eudaldo and M. Ribas (2004). "Comparison study of MOSFET detectors and diodes for entrance in vivo dosimetry in 18 MV x-ray beams." Medical physics **31**(9): 2534-2542.

Kainz, K. (2006). "Radiation oncology physics: a handbook for teachers and students." Medical Physics **33**(6): 1920-1920.

Kaus, M. R., T. Netsch, S. Kabus, V. Pekar, T. McNutt and B. Fischer (2004). Estimation of organ motion from 4D CT for 4D radiation therapy planning of lung cancer. International Conference on Medical Image Computing and Computer-Assisted Intervention, Springer.

Keall, P., A. Todor, S. Vedam, C. Bartee, J. Siebers, V. Kini and R. Mohan (2004). "On the use of EPID-based implanted marker tracking for 4D radiotherapy." Medical physics **31**(12): 3492-3499.

Kim, C., T. N. Erpelding, L. Jankovic, M. D. Pashley and L. V. Wang (2010). "Deeply penetrating in vivo photoacoustic imaging using a clinical ultrasound array system." Biomedical Optics Express **1**(1): 278-284.

Kim, J., S. An, S. Ahn and B. Kim (2013). "Depth-variant deconvolution of 3D widefield fluorescence microscopy using the penalized maximum likelihood estimation method." Optics Express **21**(23): 27668-27681.

Kim, J., E. Park, Y. Jung, B. C. Kim, J. H. Kim, C. Yi, I. J. Kim and C. Kim (2017). "X-Ray Acoustic-Based Dosimetry Using a Focused Ultrasound Transducer and a Medical Linear Accelerator." IEEE Transactions on Radiation and Plasma Medical Sciences **1**(6): 534-540.

Kim, K., L. A. Johnson, C. Jia, J. C. Joyce, S. Rangwalla, P. D. R. Higgins and J. M. Rubin (2008). "Noninvasive Ultrasound Elasticity Imaging (UEI) of Crohn's Disease: Animal Model." Ultrasound in medicine & biology **34**(6): 902-912.

Kruger, R. A., K. K. Kopecky, A. M. Aisen, D. R. Reinecke, G. A. Kruger and W. L. Kiser (1999). "Thermoacoustic CT with Radio Waves: A Medical Imaging Paradigm." Radiology **211**(1): 275-278.

Kruger, R. A., P. Liu, Y. R. Fang and C. R. Appledorn (1995). "Photoacoustic ultrasound (PAUS)—Reconstruction tomography." Medical Physics **22**(10): 1605-1609.

Ku, G. and L. V. Wang (2001). "Scanning microwave-induced thermoacoustic tomography: Signal, resolution, and contrast." Medical Physics **28**(1): 4-10.

Lai, P., X. Xu and L. V. Wang (2014). "Dependence of optical scattering from Intralipid in gelatin-gel based tissue-mimicking phantoms on mixing temperature and time." Journal of biomedical optics **19**(3): 35002-35002.

Lawrance, I. C., C. J. Welman, P. Shipman and K. Murray (2009). "Correlation of MRI-determined small bowel Crohn's disease categories with medical response and surgical pathology." World Journal of Gastroenterology : WJG **15**(27): 3367-3375.

Lehnert, S. (2008). Biomolecular action of ionizing radiation. New York, Taylor & Francis.

Lei, H., L. A. Johnson, S. Liu, D. S. Moons, T. Ma, Q. Zhou, M. D. Rice, J. Ni, X. Wang and P. D. Higgins (2016). "Characterizing intestinal inflammation and fibrosis in Crohn's disease by photoacoustic imaging: feasibility study." Biomedical optics express **7**(7): 2837-2848.

Li, C., J.-M. Yang, R. Chen, C.-H. Yeh, L. Zhu, K. Maslov, Q. Zhou, K. Kirk Shung and L. V. Wang (2014). "Urogenital photoacoustic endoscope." Optics Letters **39**(6): 1473-1476.

Li, G., D. Citrin, K. Camphausen, B. Mueller, C. Burman, B. Mychalczak, R. W. Miller and Y. Song (2008). "Advances in 4D medical imaging and 4D radiation therapy." Technology in cancer research & treatment **7**(1): 67-81.

Li, M.-L., H. F. Zhang, K. Maslov, G. Stoica and L. V. Wang (2006). "Improved in vivo photoacoustic microscopy based on a virtual-detector concept." Optics Letters **31**(4): 474-476.

Liao, C. K., M. L. Li and P. C. Li (2004). "Optoacoustic imaging with synthetic aperture focusing and coherence weighting." Optics Letters **29**(21): 2506-2508.

Liauw, S. L., P. P. Connell and R. R. Weichselbaum (2013). "New paradigms and future challenges in radiation oncology: an update of biological targets and technology." Science translational medicine **5**(173): 173sr172-173sr172.

Lichtenstein, G. R., A. Olson, S. Travers, R. H. Diamond, D. M. Chen, M. L. Pritchard, B. G. Feagan, R. D. Cohen, B. A. Salzberg, S. B. Hanauer and W. J. Sandborn (2006). "Factors Associated with the Development of Intestinal Strictures or Obstructions in Patients with Crohn's Disease." Am J Gastroenterol **101**(5): 1030-1038.

Ling, C. C., E. Yorke and Z. Fuks (2006). "From IMRT to IGRT: frontierland or neverland?" Radiotherapy and oncology **78**(2): 119-122.

Loftus, E. V., P. Schoenfeld and W. J. Sandborn (2002). "The epidemiology and natural history of Crohn's disease in population-based patient cohorts from North America: a systematic review." Alimentary Pharmacology & Therapeutics **16**(1): 51-60.

Lomax, M. E., L. K. Folkes and P. O'Neill (2013). "Biological Consequences of Radiation-induced DNA Damage: Relevance to Radiotherapy." Clinical Oncology **25**(10): 578-585.

Mans, A., P. Remeijer, I. Olaciregui-Ruiz, M. Wendling, J.-J. Sonke, B. Mijnheer, M. van Herk and J. C. Stroom (2010). "3D Dosimetric verification of volumetric-modulated arc therapy by portal dosimetry." Radiotherapy and Oncology **94**(2): 181-187.

Mascarenhas, S., H. Vargas and C. L. Cesar (1984). "A photoacoustical radiation dosimeter." Medical physics **11**(1): 73-74.

Maslov, K. I. and L. V. Wang (2008). Photoacoustic imaging of biological tissue with intensity-modulated continuous-wave laser, SPIE.

Messmann, H., E. Endlicher, G. Freunek, P. Rümmele, J. Schölmerich and R. Knüchel (2003). "Fluorescence endoscopy for the detection of low and high grade dysplasia in ulcerative colitis using systemic or local 5-aminolaevulinic acid sensitisation." Gut **52**(7): 1003-1007.

Mijnheer, B., S. Beddar, J. Izewska and C. Reft (2013). "In vivo dosimetry in external beam radiotherapy." Medical physics **40**(7).

Mijnheer, B., I. Olaciregui-Ruiz, R. Rozendaal, J. Sonke, H. Spreeuw, R. Tielenburg, M. Van Herk, R. Vijlbrief and A. Mans (2013). 3D EPID-based in vivo dosimetry for IMRT and VMAT. Journal of Physics: Conference Series, IOP publishing.

Molloy, J. A., G. Chan, A. Markovic, S. McNeeley, D. Pfeiffer, B. Salter and W. A. Tome (2011). "Quality assurance of U.S.-guided external beam radiotherapy for prostate cancer: Report of AAPM Task Group 154." Medical Physics 38(2): 857-871.

Oberhuber, G., P. C. Stangl, H. Vogelsang, E. Schober, F. Herbst and C. Gasche (2000). "Significant association of strictures and internal fistula formation in Crohn's disease." Virchows Archiv 437(3): 293-297.

Oh, J.-T., M.-L. Li, H. F. Zhang, K. Maslov and L. V. Wang (2006). "Three-dimensional imaging of skin melanoma in vivo by dual-wavelength photoacoustic microscopy." Journal of biomedical optics 11(3): 034032.

Oncology, A. S. f. R. (2008). Fast facts about radiation therapy.

Paolantonio, P., R. Ferrari, F. Vecchietti, S. Cucchiara and A. Laghi (2009). "Current status of MR imaging in the evaluation of IBD in a pediatric population of patients." European Journal of Radiology 69(3): 418-424.

Park, J., S. Jeon, J. Meng, L. Song, J. S. Lee and C. Kim (2016). Delay-multiply-and-sum-based synthetic aperture focusing in photoacoustic microscopy, SPIE.

Pasquini, C. (2003). "Near infrared spectroscopy: fundamentals, practical aspects and analytical applications." Journal of the Brazilian chemical society 14(2): 198-219.

Podgorsak, E. B. (2003). "Review of radiation oncology physics: a handbook for teachers and students." Vienna, International Atomic Energy Agency. Educational reports series.

Podgoršak, E. B. (2006). Radiation physics for medical physicists, Springer.

Qureshi, W. A. (2004). "Current and future applications of the capsule camera." Nat Rev Drug Discov 3(5): 447-450.

Ramaseshan, R., K. Kohli, T. Zhang, T. Lam, B. Norlinger, A. Hallil and M. Islam (2004). "Performance characteristics of a microMOSFET as an in vivo dosimeter in radiation therapy." Physics in medicine and biology 49(17): 4031.

Richards-Kortum, R. and E. Sevick-Muraca (1996). "QUANTITATIVE OPTICAL SPECTROSCOPY FOR TISSUE DIAGNOSIS." Annual Review of Physical Chemistry 47(1): 555-606.

Rupitsch, S. J., F. Maier and B. G. Zagar (2006). Synthetic Aperture Focusing Technique in High - Frequency Ultrasound Imaging to Locate Layer Delamination. 2006 IEEE Instrumentation and Measurement Technology Conference Proceedings.

Sandler, H. M., P. W. McLaughlin, R. K. Ten Haken, H. Addison, J. Forman and A. Lichter (1995). "Three dimensional conformal radiotherapy for the treatment of prostate cancer: low risk of chronic rectal morbidity observed in a large series of patients." International Journal of Radiation Oncology• Biology• Physics **33**(4): 797-801.

Shah, J., S. Park, S. R. Aglyamov, T. Larson, L. Ma, K. V. Sokolov, K. P. Johnston, T. E. Milner and S. Y. Emelianov (2008). Photoacoustic imaging and temperature measurement for photothermal cancer therapy, SPIE.

Shanshan, T., Y. Kai, C. Yong and X. Liangzhong (2018). "X-ray-induced acoustic computed tomography for 3D breast imaging: A simulation study." Medical Physics **45**(4): 1662-1672.

Shen, B., G. Zuccaro Jr, T. L. Gramlich, N. Gladkova, P. Trolli, M. Kareta, C. P. Delaney, J. T. Connor, B. A. Lashner, C. L. Bevins, F. Feldchtein, F. H. Remzi, M. L. Bambrick and V. W. Fazio (2004). "In vivo colonoscopic optical coherence tomography for transmural inflammation in inflammatory bowel disease." Clinical Gastroenterology and Hepatology **2**(12): 1080-1087.

Sterzing, F., R. Engenhart-Cabillic, M. Flentje and J. Debus (2011). "Image-guided radiotherapy: a new dimension in radiation oncology." Deutsches Aerzteblatt International **108**(16): 274.

Steven, L. J. (2013). "Optical properties of biological tissues: a review." Physics in Medicine and Biology **58**(11): R37.

Stewart, R. D. and X. A. Li (2007). "BGRT: Biologically guided radiation therapy—The future is fast approaching!" Medical Physics **34**(10): 3739-3751.

Stidham, R. W. and P. D. R. Higgins (2016). "Imaging of intestinal fibrosis: current challenges and future methods." United European Gastroenterology Journal **4**(4): 515-522.

Stidham, R. W., J. Xu, L. A. Johnson, K. Kim, D. S. Moons, B. J. McKenna, J. M. Rubin and P. D. Higgins (2011). "Ultrasound elasticity imaging for detecting intestinal fibrosis and inflammation in rats and humans with Crohn's disease." Gastroenterology **141**(3): 819-826 e811.

Tada, J., Y. Hayakawa, K. Hosono and T. Inada (1991). "Time resolved properties of acoustic pulses generated in water and in soft tissue by pulsed proton beam irradiation—A possibility of doses distribution monitoring in proton radiation therapy." Medical physics **18**(6): 1100-1104.

Tang, S., D. H. Nguyen, A. Zarafshani, C. Ramseyer, B. Zheng, H. Liu and L. Xiang (2017). "X-ray-induced acoustic computed tomography with an ultrasound transducer ring-array." Applied Physics Letters **110**(10): 103504.

Tarján, Z., G. Tóth, T. Györke, Á. Mester, K. Karlinger and E. K. Makó (2000). "Ultrasound in Crohn's disease of the small bowel." European Journal of Radiology **35**(3): 176-182.

Tarvainen, T., M. Vauhkonen, V. Kolehmainen and J. P. Kaipio (2006). "Finite element model for the coupled radiative transfer equation and diffusion approximation." International Journal for Numerical Methods in Engineering **65**(3): 383-405.

Tian, C., Z. Xie, M. L. Fabiilli, S. Liu, C. Wang, Q. Cheng and X. Wang (2015). "Dual-pulse nonlinear photoacoustic technique: a practical investigation." Biomedical Optics Express **6**(8): 2923-2933.

Timmerman, R. D. and L. Xing (2012). Image-guided and adaptive radiation therapy, Lippincott Williams & Wilkins.

Treeby, B. E. and B. T. Cox (2010). k-Wave: MATLAB toolbox for the simulation and reconstruction of photoacoustic wave fields, SPIE.

van Elmpt, W., L. McDermott, S. Nijsten, M. Wendling, P. Lambin and B. Mijnheer (2008). "A literature review of electronic portal imaging for radiotherapy dosimetry." Radiotherapy and Oncology **88**(3): 289-309.

Van Herk, M. (2004). Errors and margins in radiotherapy. Seminars in radiation oncology, Elsevier.

Wang, H.-W., N. Chai, P. Wang, S. Hu, W. Dou, D. Umulis, L. V. Wang, M. Sturek, R. Lucht and J.-X. Cheng (2011). "Label-Free Bond-Selective Imaging by Listening to Vibrationally Excited Molecules." Physical Review Letters **106**(23): 238106.

Wang, L., S. L. Jacques and L. Zheng (1995). "MCML—Monte Carlo modeling of light transport in multi-layered tissues." Computer Methods and Programs in Biomedicine **47**(2): 131-146.

Wang, L., C. Zhang and L. V. Wang (2014). "Grueneisen Relaxation Photoacoustic Microscopy." Physical Review Letters **113**(17): 174301.

Wang, L. V. (2009). "Multiscale photoacoustic microscopy and computed tomography." Nature Photonics **3**: 503.

Wang, L. V. and S. Hu (2012). "Photoacoustic Tomography: In Vivo Imaging from Organelles to Organs." Science **335**(6075): 1458-1462.

Wang, X., D. R. Bauer, R. Witte and H. Xin (2012). "Microwave-Induced Thermoacoustic Imaging Model for Potential Breast Cancer Detection." IEEE Transactions on Biomedical Engineering **59**(10): 2782-2791.

Wang, X., Y. Pang, G. Ku, G. Stoica and L. V. J. O. l. Wang (2003). "Three-dimensional laser-induced photoacoustic tomography of mouse brain with the skin and skull intact." **28**(19): 1739-1741.

Wang, X., Y. Pang, G. Ku, X. Xie, G. Stoica and L. V. Wang (2003). "Noninvasive laser-induced photoacoustic tomography for structural and functional in vivo imaging of the brain." Nature Biotechnology **21**: 803.

Webb, S. (2001). Intensity-modulated radiation therapy, CRC Press.

Welch, A. J. and M. J. Van Gemert (2011). Optical-thermal response of laser-irradiated tissue, Springer.

Xia, J., J. Yao and L. V. Wang (2014). "Photoacoustic tomography: principles and advances." Electromagnetic waves (Cambridge, Mass.) **147**: 1-22.

Xiang, L., B. Han, C. Carpenter, G. Pratx, Y. Kuang and L. Xing (2013). "X-ray acoustic computed tomography with pulsed x-ray beam from a medical linear accelerator." Medical physics **40**(1).

Xiang, L., S. Tang, M. Ahmad and L. Xing (2016). "High Resolution X-ray-Induced Acoustic Tomography." Scientific Reports **6**: 26118.

Xing, L., B. Thorndyke, E. Schreibmann, Y. Yang, T.-F. Li, G.-Y. Kim, G. Luxton and A. Koong (2006). "Overview of image-guided radiation therapy." Medical Dosimetry **31**(2): 91-112.

Xu, M. and L. V. Wang (2005). "Universal back-projection algorithm for photoacoustic computed tomography." Physical Review E **71**(1): 016706.

Xu, M. and L. V. Wang (2006). "Photoacoustic imaging in biomedicine." Review of Scientific Instruments **77**(4): 041101.

Yang, J.-M., R. Chen, C. Favazza, J. Yao, C. Li, Z. Hu, Q. Zhou, K. K. Shung and L. V. Wang (2012). "A 2.5-mm diameter probe for photoacoustic and ultrasonic endoscopy." Optics Express **20**(21): 23944-23953.

Yang, J.-M., C. Favazza, R. Chen, J. Yao, X. Cai, K. Maslov, Q. Zhou, K. K. Shung and L. V. Wang (2012). "Simultaneous functional photoacoustic and ultrasonic endoscopy of internal organs in vivo." Nat Med **18**(8): 1297-1302.

Yang, J.-M., C. Li, R. Chen, Q. Zhou, K. K. Shung and L. V. Wang (2014). "Catheter-based photoacoustic endoscope." Journal of Biomedical Optics **19**(6): 066001-066001.

Yang, J.-M., K. Maslov, H.-C. Yang, Q. Zhou, K. K. Shung and L. V. Wang (2009). "Photoacoustic endoscopy." Optics Letters **34**(10): 1591-1593.

Yang, J. M., C. Favazza, J. Yao, R. Chen, Q. Zhou, K. K. Shung and L. V. Wang (2015). "Three-Dimensional Photoacoustic Endoscopic Imaging of the Rabbit Esophagus." PLOS ONE **10**(4): e0120269.

Yang, V. X. D., S.-j. Tang, M. L. Gordon, B. Qi, G. Gardiner, M. Cirocco, P. Kortan, G. B. Haber, G. Kandel, I. A. Vitkin, B. C. Wilson and N. E. Marcon (2005). "Endoscopic Doppler optical coherence tomography in the human GI tract: initial experience." Gastrointestinal Endoscopy **61**(7): 879-890.

Yao, D.-K., K. Maslov, K. K. Shung, Q. Zhou and L. V. Wang (2010). "In vivo label-free photoacoustic microscopy of cell nuclei by excitation of DNA and RNA." Optics Letters **35**(24): 4139-4141.

Yao, D.-K., C. Zhang, K. Maslov and L. V. Wang (2014). "Photoacoustic measurement of the Grüneisen parameter of tissue." Journal of biomedical optics **19**(1): 17007-17007.

Yi, W., X. Da, Z. Yaguang and C. Qun (2004). "Photoacoustic imaging with deconvolution algorithm." Physics in Medicine & Biology **49**(14): 3117.

Yu, C., C. Zhang and L. Xie (2012). "A blind deconvolution approach to ultrasound imaging." IEEE Transactions on Ultrasonics, Ferroelectrics, and Frequency Control **59**(2): 271-280.

Zhang, C., K. I. Maslov, S. Hu, L. V. Wang, R. Chen, Q. Zhou and K. K. Shung (2012). Reflection-mode submicron-resolution *in vivo* photoacoustic microscopy, SPIE.

Zhang, H. F., K. Maslov, G. Stoica and L. V. Wang (2006). "Functional photoacoustic microscopy for high-resolution and noninvasive in vivo imaging." Nature Biotechnology **24**: 848.

Zhou, Y., J. Yao and L. V. Wang (2016). Tutorial on photoacoustic tomography, SPIE.

Zhu, Y., L. A. Johnson, Z. Huang, J. M. Rubin, J. Yuan, H. Lei, J. Ni, X. Wang, P. D. R. Higgins and G. Xu (2018). "Identifying intestinal fibrosis and inflammation by spectroscopic photoacoustic imaging: an animal study in vivo." Biomedical Optics Express **9**(4): 1590-1600.